On-site Synthesis of Halide Perovskite Nanocrystals with Sub-50 nm Positional Accuracy

by

Patricia Jastrzebska-Perfect

B.S., Columbia University (2020)

Submitted to the Department of Electrical Engineering and Computer Science
in partial fulfillment of the requirements for the degree of

Master of Science in Electrical Engineering and Computer Science

at the

MASSACHUSETTS INSTITUTE OF TECHNOLOGY

May 2022

Author .....
Department of Electrical Engineering and Computer Science
May 13, 2022

Certified by .....
Farnaz Niroui
Assistant Professor of Electrical Engineering and Computer Science
Thesis Supervisor

Accepted by .....
Leslie A. Kolodziejski
Professor of Electrical Engineering and Computer Science
Chair, Department Committee on Graduate Students

On-site Synthesis of Halide Perovskite Nanocrystals with Sub-50 nm Positional Accuracy

by

Patricia Jastrzebska-Perfect

Submitted to the Department of Electrical Engineering and Computer Science
on May 13, 2022, in partial fulfillment of the
requirements for the degree of
Master of Science in Electrical Engineering and Computer Science

Abstract

Metal halide perovskites comprise a promising class of semiconductors with broad applications ranging from optoelectronics and photovoltaics to photocatalysis. To extend these applications to on-chip devices, on-site growth of perovskite nanocrystals with high positional accuracy must be achieved. In this thesis, we demonstrate a method for growing sub-50 nm halide perovskite nanocrystals with sub-50 nm positional accuracy. We first explore how local forces can be engineered to control particle positioning at the nanoscale. We then show how our parameters of control - namely template geometry and solvent contact angle - can be utilized to position nanocrystals within lithographic templates. This thesis reveals a unique strategy that overcomes the limitations of conventional lithographic processes for high-resolution growth of halide perovskites.

Thesis Supervisor: Farnaz Niroui
Title: Assistant Professor of Electrical Engineering and Computer Science

Acknowledgments

I first thank my advisor, Farnaz Niroui, for her guidance, mentorship, and encouragement over the past two years, and for fostering a research environment that has pushed me to become a better scientist.

I further thank my colleagues in the Niroui Group (Spencer, Peter, and Sarah) and ONE Lab (Roberto and Mayuran) for their advice, assistance, and camaraderie throughout all stages of this work.

I also acknowledge the late Alan L. McWhorter, who supported this work through a departmental fellowship, and the National Science Foundation, which supported this work through a Graduate Research Fellowship under Grant No. 1745302.

Finally, I thank my family and friends for their boundless support, without which I could not have reached this point.

Contents

List of Figures

List of Tables

Chapter 1

Introduction

Metal halide perovskites (MHPs) have received significant research interest in recent years due to their attractive optoelectronic characteristics. To ultimately enable their device integration, perovskite micro and nanocrystals must be patterned on or around optical and electrical structures. However, the intrinsic properties of perovskites render them incompatible with conventional micro and nanofabrication methodologies, necessitating the investigation of new patterning strategies.

In this thesis, I will present a method for guided growth of MHP nanocrystals with sub-50 nm positional accuracy. In Chapter 2, I will review the properties of MHPs, and discuss existing methods of patterning them. Further, I will demonstrate the necessity for a high-positional accuracy patterning technique. In Chapter 3, I will present how asymmetric menisci can be formed within lithographically-defined templates, yielding pressure gradients that can be applied for nanocrystal positioning. In Chapter 4, I will show experimental results demonstrating on-site growth of $CsPbBr_3$ nanocrystals with high-positional accuracy. Finally, in Chapter 5, I will discuss future directions for the work.

Chapter 2

Metal halide perovskites

This chapter will introduce the properties of metal halide perovskites (MHPs), and explore the existing methods for patterning these materials. Further, this chapter will present the limitations of fabrication approaches, and motivate the need for a patterning technique that enables on-site growth of crystals with high positional accuracy.

2.1 Properties of MHPs

Metal halide perovskites assume the general formula ABX_3, and are classified as either organic-inorganic or all-inorganic, depending on whether an organic cation, like methylammonium (MA, $CH_3NH_3^+$) or formamidinium (FA, $CH(NH_2)_2^+$)), or inorganic cation, like Cs^+ or Rb^{2+}, occupies the A-site. The B-site is occupied by a divalent metal cation like Pb^{2+}, Sn^{2+}, or Ge^{2+}. Finally, the X-site is occupied by one or more halides, like Br^-, Cl^- or I^-. The perovskite crystal structure comprises a 3D network of A-site cations interspersed between $[BX_6]^{4-}$ octahedra. As Fig. 2-1 demonstrates, A-site cations are 12-fold coordinated, and located in the middle of 8 corner-sharing $[BX_6]^{4-}$ octahedra. Perovskites typically adopt the depicted cubic structure at higher temperatures, and display a tilted (e.g. orthorhombic or tetragonal) structure at lower temperatures [1].

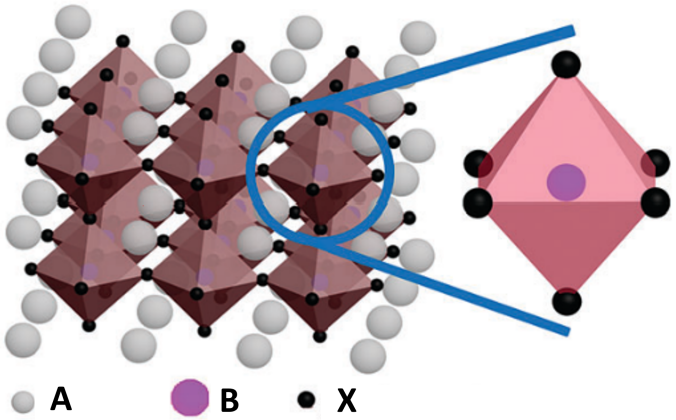

Figure 2-1. Schematic representation of cubic MHP crystal. Adapted from [1].

Perovskites are known for their superior optoelectronic properties, which predispose perovskites for use within optoelectronic devices like solar cells, photodetectors, or light-emitting diodes (LEDs). Some of these properties are summarized below:

- Perovskites display **high absorption coefficients** relative to conventional semiconductors like GaAs [5, 6]. This characteristic makes perovskites useful for light-absorbing devices, since thinner absorber layers can be used without compromising device efficiency. For example, while a $MAPbI_3$-based solar cell with a 0.3 μm absorber layer displays a maximum efficiency of 21%, a similar GaAs-based cell only displays a 13% maximum efficiency [5].

- Perovskites display relatively **low defect densities**, especially given their ease-of-processing.[1] For instance, to achieve a non-radiative recombination coefficient A of order 10^7 s^{-1} with conventional semiconductors, growth conditions would need to be carefully controlled using sophisticated techniques. By contrast, a similar A could be achieved using low-cost deposition techniques with MHPs [7]. This property suggests that perovskites can be used to create high-performance optoelectronic devices under less

[1] In the literature, perovskites may also be referred to as "defect-tolerant," meaning their defects do not serve as strong non-radiative recombination centers. However, emergent work suggests that the A for halide perovskites is actually comparable to or greater than that for conventional semiconductors, thus bringing into question the correctness of the term [7]. The term "defect-tolerant" is therefore avoided here.

demanding conditions.

- Nanocrystals of perovskites demonstrate high photoluminescence quantum yields (PLQYs), with some synthesis methods yielding **near-unity PLQYs** [8]. This property suggests that perovskites can be used within high-efficiency devices.

While these properties establish perovskites as a favorable class of semiconductors, one optoelectronic property - facile band gap tunability - fully distinguishes perovskites from their conventional semiconductor counterparts. The factors enabling band gap tunability are summarized here:

- **Composition:** As halide ion size decreases, perovskite band gap increases. For example, while the bandgap of cubic $CsPbI_3$ is 1.76 eV, the band gap of cubic $CsPbBr_3$ is 2.26 eV, and that of cubic $CsPbCl_3$ is 2.85 eV [1]. By mixing and adjusting the relative ratios of different halides (i.e. Cl/Br, or Br/I), the band gap of MHPs can be tuned across the entire visible spectrum [9].

- **Structure:** Perovskite structure, including phase, also affects bandgap. If the band gaps of different phases of one composition are compared at the same temperature (which is 0 K for comparisons made via density functional theory), the cubic phase will generally display the smallest band gap, since the unit cell displays the least degree of octahedral tilting.[2]

- **Size:** Like other semiconductors, perovskites display an increased band gap at quantum confined dimensions. From the Brus model, the effective band gap for a (spherical) quantum dot (QD) is given by

$$E_{eff} \approx E_g + \frac{\hbar^2 \pi^2}{2R^2}\left[\frac{1}{m_e} + \frac{1}{m_h}\right] - \frac{1.8e^2}{\epsilon R} \tag{2.1}$$

  where E_g is the band gap of bulk material, R is the radius of the QD, m_e and m_h are the effective masses of the electron and hole, respectively, and ϵ is the

[2]This effect therefore contributes to the band gap of $CsPbBr_3$ (orthorhombic at room temperature, RT), being higher than that of $MAPbBr_3$ or $FAPbBr_3$ (cubic at RT) [10].

dielectric constant of the semiconductor [11]. This equation states that band gap of a quantum dot is higher than that of bulk due to exciton confinement and Coulombic interaction between the electron and hole (i.e. exciton binding). Since the confinement term is a function of R^2 and Coulombic interaction term is a function of R, the net effect of radius decreasing is E_{eff} increasing. Eqn. 2.1 applies when the dimensions of the crystal are comparable to or smaller than exciton Bohr diameter. For $CsPbX_3$ perovskites, the diameters are $d_{Cl} = 5$ nm, $d_{Br} = 7$ nm, and $d_I = 12$ nm, where d_X represents the exciton Bohr diameter for $CsPbX_3$ [9]. These diameters agree with experimental results that show the emission of $CsPbBr_3$ nanocrystals increases from 2.42 eV to 2.55 eV as crystal diameter reduces from 11.8 nm to 6.6 nm [9].

In contrast with other semiconductors, perovskites demonstrate a size-correlated emission blue-shift even for crystals not of quantum-confined dimensions. It has been reported that as the lateral size of $MAPbBr_3$ single crystals decreases from 460 nm to 110 nm (which corresponds to thickness decreasing from 150 nm to 40 nm), the energy of the photoluminescence (PL) peak increases by 26 meV. This size-dependent energy shift has been attributed to the presence of defects at the crystal surface that yield emission of excitons of varying energies, whereby larger crystals reabsorb the photons emitted by higher-energy emission modes more effectively than small crystals do [12].

2.2 Growth of perovskites

2.2.1 Growth mechanisms

Perovskite thin films or crystals are grown via solution-phase, vapor-phase, or mixed approaches. Solution-phase growth of perovskites is based upon controlled crystallization. First, a precursor solution is prepared by dissolving salts of perovskite precursors in polar aprotic solvents (e.g. dimethyl sulfoxide (DMSO) or dimethylformamide (DMF)). If that solution is then brought to supersaturation, like

by changing temperature, evaporating solvent, or adding anti-solvents, nucleation and subsequent crystal growth will occur [13]. To perform solution-phase growth of perovskites on a substrate, the precursor solution is deposited by spin-coating, blade-coating, or ink-jet printing. Subsequent processing steps (e.g. depositing anti-solvents, heating, etc.) are then performed to control the rate of crystallization, which affects crystal morphology and grain size.

Perovskites can also be grown in vapor-phase. For this, a substrate (i.e a template for epitaxy) is placed into a physical or chemical vapor deposition chamber; precursors then deposit in gaseous phase on the substrate [13]. Vapor-phase deposition can also be combined with solution-phase deposition, whereby a seed crystal may be grown via solution-phase and then converted to perovskite via vapor-phase reactions [14].

2.2.2 Patterning approaches

Patterning techniques can be categorized as "top-down" or "bottom-up" (Fig. 2-2). Top-down approaches rely on selectively damaging or removing material from regions of pre-grown perovskite films, thus forming patterns out of the material that is left behind. Such patterning has been accomplished via focus-ion beam milling, laser-ablation, e-beam lithography, or photolithography [13]. While top-down

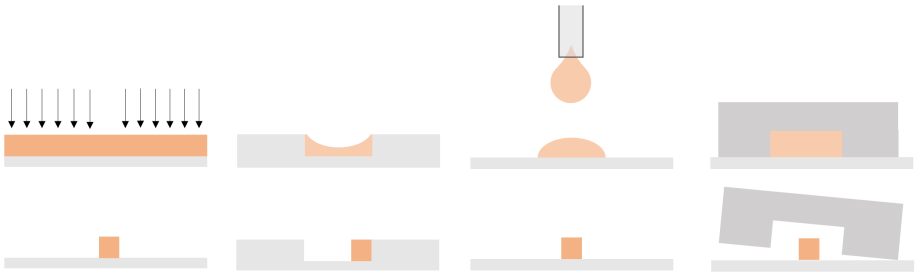

Figure 2-2. Examples of perovskite patterning approaches. From left to right: ion beam milling, template-based confinement, local solution deposition, mold-based confinement.

approaches offer ease-of-patterning, they require processing steps that are not compatible with perovskites and can degrade perovskite properties. Bottom-up approaches, which enable growth of perovskites directly on substrates through

spatial confinement of precursor solutions, are therefore more suited for device-integration. In these methods, spatial confinement is achieved via physical and/or chemical means. For example, He and colleagues formed arrays of $CsPbX_3$ microcrystals by pressing a polydimethylsiloxane (PDMS) mold onto a substrate with a droplet of precursor solution, thus forming local reservoirs of precursor solution that guided crystal growth [15]. Feng et al. used silicon micropillars with wetting top-surfaces and non-wetting sides as a "liquid knife" that split a film of precursor liquid into microdomains, thus forming a $MAPbBr_3$ crystal at the site of each micropillar [16]. Wang et al. showed that PbI_2 seeds could form within the wetting-wells of a lithographically-patterned template; these seeds could then be transformed to $MAPbI_3$ under MAI vapor [17]. Similarly, Lin et al. used mixed-wetting templates to form arrays of CsX seeds, which were transformed to $CsPbX_3$ crystals of sizes ranging from 200 nm to 1 μm through appropriate vapors [14]. The hereto smallest locally-grown perovskite nanocrystals were demonstrated by Mirkin and colleagues, who produced crystals as small as 50 nm by using polymer pen lithography to confine the precursor solution [12].

Though existing bottom-up approaches have enabled localized growth of perovskite nanocrystals, these approaches have not allowed for growth with high (e.g. nanoscale) positional accuracy, which would be required for realization of on-chip, nanoscale devices. In the bottom-up approaches, positional accuracy is determined by dimensions of the confining region. For example, if precursor solution is deposited via polymer pen lithography, positional accuracy, defined as mean displacement from chosen reference point, is limited by the radius of the droplet on the substrate [12]. (Droplet radius is a function of droplet volume and the precursor solution's contact angle with the underlying substrate; the radius therefore has physically-imposed minimum value). If confinement is instead achieved via topographical templates, positional accuracy is determined by the size of the lithographically-patterned well. While decreasing the lateral dimensions of a well would reduce the extent of displacement possible to improve positional accuracy, smaller wells would not necessarily contain sufficient precursor solution to form

particles of a desired size (see Appendix A). Further, while altering the vertical geometry of the well could improve positional control [18], such a technique could not easily be applied for fabrication of perovskite-based devices, as particles would be located deep within wells etched into a crystalline substrate. For devices to be miniaturized to the nanoscale, a new bottom-up approach that overcomes the existing positional-accuracy limits must be developed.

Chapter 3

Asymmetric menisci for particle positioning

3.1 Introduction

This chapter will examine whether asymmetric menisci can be utilized to precisely position particles within wells. First, we will review the shape that menisci take on during drainage of capillaries, and introduce the concepts of the "arc meniscus" and "disjoining pressure." Next, we will consider how meniscus asymmetries can yield pressure gradients within wells. Finally, we will explore how well geometry can be applied to control arc menisci, and thus create asymmetric menisci for particle positioning.

3.1.1 Menisci during drainage

In this section, we will review the shape of a meniscus when liquid drains from a capillary. This review will inform the concept of the "arc meniscus," an idea that will later be applied when discussing creation of asymmetric menisci.

A Meniscus in arbitrary cylinder

First, consider the meniscus formed in an arbitrarily-shaped cylinder. Fig. 3-1 presents a cylinder of arbitrary cross-section Ω and perimeter Σ that is partially filled with a wetting fluid. The contact-angle the fluid makes with the sidewalls of the cylinder is given by θ. We want to find a surface $S = u(x, y)$ of constant curvature, which covers Ω and intersects the cylinder walls at contact angle $0 < \theta < \pi/2$. However, a solution S that yields a meniscus of singular height (whereby height is constant for all points on Σ) only exists when $\theta_c < \theta < \pi/2$, where θ_c is the critical angle [2]. Therefore, liquid will remain in Ω^* provided

$$0 < \theta < \theta_c \tag{3.1}$$

The liquid that remains in the cross section Ω^* is referred to as the "arc meniscus" (AM). Further, the liquid that exists in $\Omega - \Omega^*$ is denoted the "main terminal meniscus" (MTM).

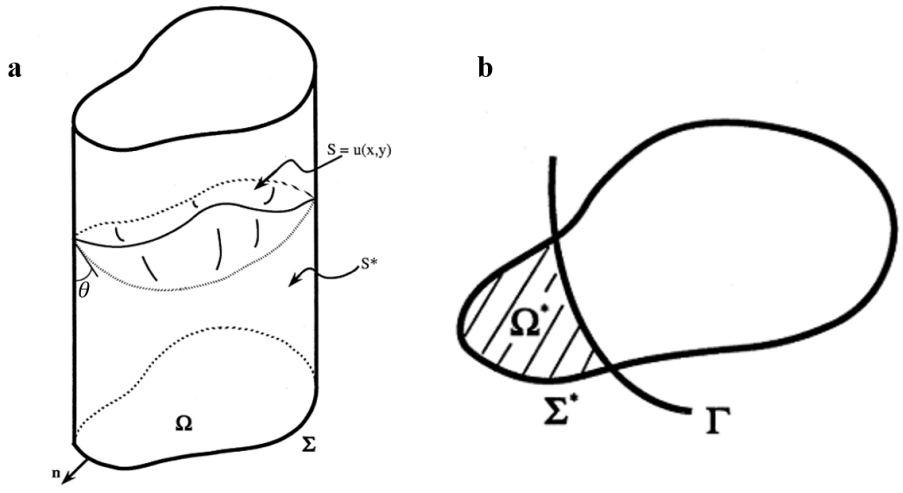

Figure 3-1. (a) Generic cylinder of cross section Ω and perimeter Σ that is partially filled with wetting fluid. (b) Top view of cylinder of cross section Ω showing liquid in Ω^*. Adapted from [2].

B Meniscus in polygonal capillary

The arc and main terminal menisci can be better understood through a polygonal capillary. Consider Fig. 3-2, which depicts a triangular capillary initially filled with wetting phase. During the drainage process, the non-wetting phase invades the bulk and the MTM propagates into the capillary like a finger. The MTM maintains a spherical shape due to absence of gravitational forces (see Appendix B). However, as the MTM propagates, some quantity of wetting phase - the AM - remains in the corners. Zero gravitational force mandates constant curvature, so the curvature of the main terminal meniscus matches that of the arc menisci [19]. These same processes occur whether drainage results from liquid flowing out of the bottom of the capillary, or from liquid evaporating from the top of the capillary [20].

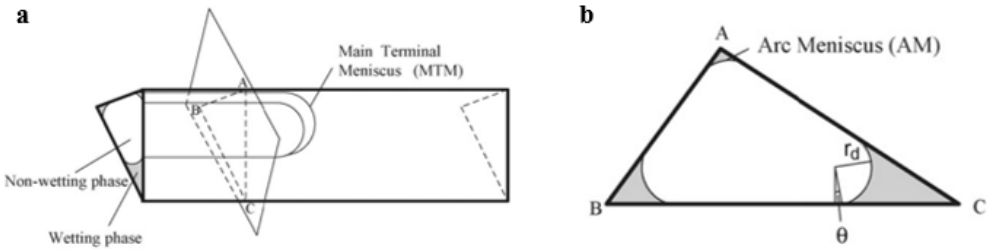

Figure 3-2. (a) Triangular tube containing wetting-phase that is invaded by non-wetting phase during drainage. (b) Cross-section of tube at plane identified in "a". Adapted from [3].

C Arc meniscus during drainage

From Fig. 3-1, Ω^* depends on θ and Σ^*. Therefore, both the contact angle that liquid makes with the capillary sidewalls and the geometry of the capillary affect whether the arc meniscus exists during drainage.

C.1 AM existence The condition for wetting phase remaining in the corners during drainage can be understood by considering Fig. 3-3. The wetting phase (gray) occupies the corner when the triangle outlined in red exists. Therefore, the

condition for wetting phase occupying a corner of the well is given by

$$\frac{\alpha}{2} + \phi + \theta + \frac{\pi}{2} = \pi \tag{3.2}$$

Both α, the corner angle of the well, and θ, the contact angle made by the wetting phase with the sidewall of the well, are positive ($\alpha > 0$ and $\theta > 0$). Further, for the red-outlined triangle to exist, $\phi \geq 0$. Therefore, wetting phase remains in the corner when

$$\phi = \frac{\pi}{2} - \frac{\alpha}{2} - \theta \geq 0 \tag{3.3}$$

$$\frac{\pi}{2} \geq \frac{\alpha}{2} + \theta \tag{3.4}$$

Eqn. 3.4 can be used to determine the critical contact angle θ_c, namely the contact angle at which the wetting-phase ceases to occupy the corner during drainage. θ_c is given by

$$\theta_c = \frac{\pi}{2} - \frac{\alpha}{2} \tag{3.5}$$

Combining Eqns. 3.1 and 3.5, the AM exists in the corner of a capillary during drainage provided

$$0 \leq \theta \leq \frac{\pi}{2} - \frac{\alpha}{2} \tag{3.6}$$

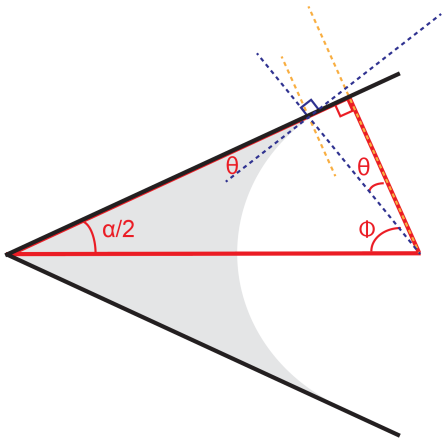

Figure 3-3. Top view of corner of well. The wetting phase (gray) occupies corner of angle α. θ is the contact angle made by wetting phase with the sidewalls of the well.

C.2 AM radius The radius of the arc meniscus for various well geometries can be analytically computed using theory presented by Jia and colleagues [3]. These equations are restated here, as they will be referenced later.

Triangular well Consider a triangular well formed by an isosceles triangle. Let A be the area and P the perimeter of the triangle. Further, let θ_{c_1} be the critical angle of the larger corner angle, and θ_{c_2} be the critical angle of the smaller corner angle. When $0 \leq \theta \leq \theta_{c_1}$, the AM radius r is given by

$$r = f_1(G, \theta)P \tag{3.7}$$

$$f_1(G, \theta) = \frac{2G}{\sqrt{4G(\pi - 3\theta + 3\sin\theta\cos\theta)} + \cos\theta} \tag{3.8}$$

$$G = \frac{A}{P^2} \tag{3.9}$$

When $\theta_{c_1} \leq \theta \leq \theta_{c_2}$, the AM radius r is given by

$$r = f_3(G, \theta, \alpha, \beta)P \tag{3.10}$$

$$f_3(G, \theta, \alpha, \beta) = \frac{2G}{\sqrt{4G(\frac{\alpha+\beta-2\theta}{2} + \sin\theta\cos\theta + \cos^2\theta(\cot\frac{\alpha}{2} + \cot\frac{\beta}{2}))} + \cos\theta} \tag{3.11}$$

Here, α and β are the angles of the two corners occupied by non-wetting phase. Since the triangle is isosceles, $\alpha = \beta$.

Square well Consider a square well. Let A_{eff} be the area and P_{eff} the perimeter of the AMs in all corners. Further, let A be the area and P the perimeter of the square well. When $0 \leq \theta \leq \theta_c$, the AM radius is given by

$$r = \frac{A_{eff}}{P_{eff}} \tag{3.12}$$

$$A_{eff} = A - 4r^2\cos^2\theta + \frac{2\pi - 8\theta}{2\pi}\pi r^2 + 4r^2\sin\theta\cos\theta \tag{3.13}$$

$$P_{eff} = (P - 8r\cos\theta + 8r\sin\theta)\cos\theta + \frac{2\pi - 8\theta}{2\pi}2\pi r \tag{3.14}$$

Eqns. 3.12, 3.13, and 3.14 can be simplified to find a solution in terms of r:

$$r = \frac{-b + \sqrt{b^2 - 4ac}}{2a} \tag{3.15}$$

$$a = \pi - 4\theta + 4\sin\theta\cos\theta - 4\cos^2\theta \tag{3.16}$$

$$b = P\cos\theta \tag{3.17}$$

$$c = -A \tag{3.18}$$

3.1.2 Disjoining pressure

In this section, we will review the concept of the disjoining pressure. This review will provide a basis for subsequent discussion on how pressure differences (and hence gradients) can exist within wells during drainage at the nanometer scale.

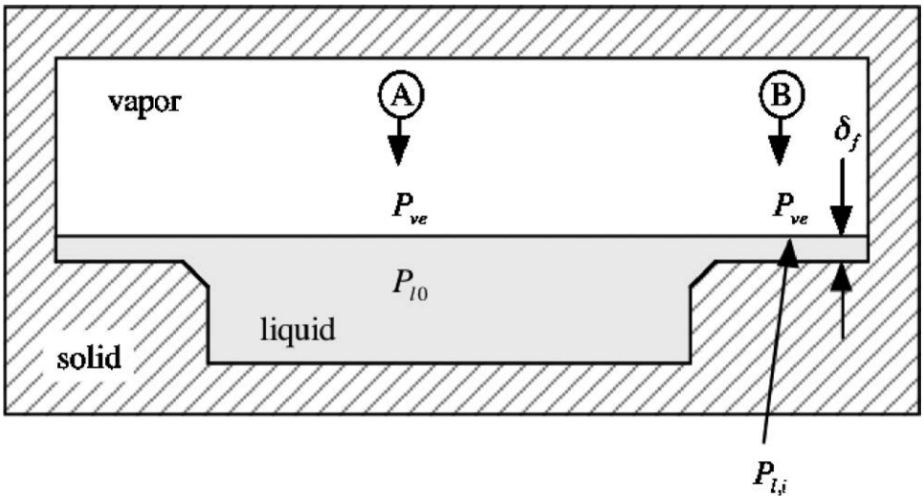

Figure 3-4. Cross-section of enclosed chamber containing liquid. Adapted from [4].

Consider Fig. 3-4, which depicts an enclosed system at equilibrium, with the liquid contained both in a bulk region and within a narrow region of height δ_f. Since the system is at equilibrium, the pressure at the bulk interface, P_{lo}, equals the vapor

pressure P_{ve}, namely $P_{lo} = P_{ve}$. However, in the thin liquid film, the pressure at the interface P_{li} is affected by the interactions of the liquid with the solid underneath.

The mean-field potential energy for a liquid molecule due to interactions with solid molecules is given by

$$\Phi_{fs} = \iiint_V \rho_s \phi_{fs} dV \tag{3.19}$$

where ϕ_{fs}, the potential between a pair of liquid-solid molecules, is modeled by the Lennard-Jones potential given by

$$\phi_{fs}(r) = \frac{-C_{\phi,fs}}{r^6}(1 - \frac{D_s^6}{r^6}) \tag{3.20}$$

Here, D_s represents the closest distance from between a liquid-solid particle pair, ρ_s is the density of solid particles within volume V, and $C_{\phi,fs}$ is an interaction parameter. For zero flow ($\vec{v} = 0$ and $\frac{D\vec{v}}{Dt} = 0$), the Navier-Stokes equation, which states

$$\rho_f \frac{D\vec{v}}{Dt} = -\nabla P + \rho_f \vec{f_b} + \mu \nabla^2 \vec{v} \tag{3.21}$$

simplifies to

$$0 = -\nabla P + \rho_f \vec{f_b} \tag{3.22}$$

where $\vec{f_b}$ is force per unit mass. Since gravitational forces are negligible at the length scale of interest (see Appendix B), the force exerted on fluid molecule by the solid, $\vec{F_b}$ results from the mean-field potential, namely

$$\vec{F_b} = -\nabla \Phi_{fs} \tag{3.23}$$

$\vec{f_b}$ is converted to $\vec{F_b}$ through

$$\vec{F_b} = \frac{M_f}{N_A} \vec{f_b} \tag{3.24}$$

where M_f is the molecular weight of the fluid, and N_A is Avogadro's number. Using these expressions, Carey and Wemhoff [4] show that the interactions between liquid-solid molecules yield a pressure gradient ∇P, which in one-dimension (z) reduces

to

$$\nabla P = \frac{dP}{dz} \tag{3.25}$$

The pressure profile $P(z)$ for $0 \leq z \leq \delta_f$ can be expressed by

$$P(z) = P_{lo} + \frac{A_{fs}}{6\pi z^3} \tag{3.26}$$

where Hamaker constant A_{fs} defines the interaction strength between a pair of liquid-solid molecules and is defined by

$$A_{fs} = \pi^2 \rho_f \rho_s C_{\phi,fs} \tag{3.27}$$

Therefore the pressure at the thin-film interface P_{li}, where $z = \delta_f$ is given by

$$P_{li} = P_{lo} + \frac{A_{fs}}{6\pi \delta_f^3} \tag{3.28}$$

This equation states that the pressure at the thin film interface is higher than the pressure in the bulk by a differential factor. This differential factor, commonly called the "disjoining pressure," corresponds to the amount by which P_{ve} differs from P_{li}, where the disjoining pressure P_d is defined by

$$P_d = P_{ve} - P_{li} = -\frac{A_{fs}}{6\pi \delta_f^3} \tag{3.29}$$

3.2 Results

Since $P_d = f(\frac{1}{z^3})$, local variations in z should produce local variations in disjoining pressure. In this section, we will show that an asymmetric meniscus, which produces local variations in z, should produce a directional pressure gradient. We will consider the direction and magnitude of resultant pressure gradient force to show that the asymmetric meniscus should help position a particle contained within the liquid. Finally, we will present well geometry as variable for forming asymmetric menisci.

3.2.1 Pressure gradient force

A Direction and magnitude

Consider Fig. 3-5, which depicts the cross-section of shallow well (i.e. order of 20 nm) containing an asymmetric meniscus. We are interested in finding the lateral gradient of pressure, defined as

$$\nabla P = \frac{dP}{dx} \tag{3.30}$$

at the two extremes of the meniscus. Let P_0 represent the pressure at y_0, P_1 the

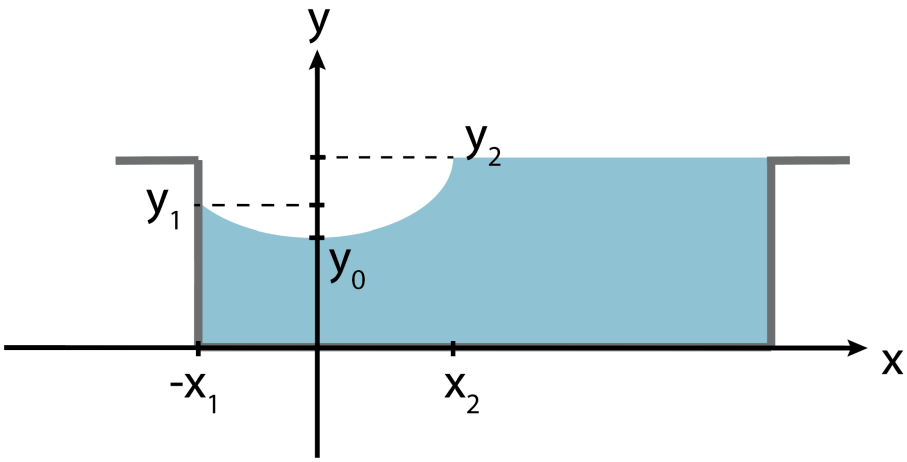

Figure 3-5. Cross-section of well displaying an asymmetric meniscus during drainage.

pressure at y_1, and P_2 the pressure at y_2. Then,

$$\nabla P_{x_1} = \frac{P_1 - P_0}{-x_1 - 0} = \frac{P_0 - P_1}{x_1} \tag{3.31}$$

$$\nabla P_{x_2} = \frac{P_2 - P_0}{x_2 - 0} = \frac{P_2 - P_0}{x_2} \tag{3.32}$$

Considering the ratio of the magnitudes of these two pressure gradients, we find

$$\frac{|\nabla P_{x_1}|}{|\nabla P_{x_2}|} = \frac{|\frac{P_0 - P_1}{x_1}|}{|\frac{P_2 - P_0}{x_2}|} = \frac{x_2}{x_1}\frac{|P_0 - P_1|}{|P_0 - P_2|} \tag{3.33}$$

Since the meniscus takes a spherical shape (see Appendix B), $x_2 \approx x_1$. Further, the well is assumed to be shallow, so Eqn. 3.29, which states that the disjoining pressure is inversely related to δ^3, applies. Therefore, since $y_0 < y_1 < y_2$, it follows that $P_2 < P_1 < P_0$. As a result,

$$0 < \frac{|\nabla P_{x_1}|}{|\nabla P_{x_2}|} < 1 \tag{3.34}$$

This means that there is a greater pressure gradient in the region defined by $[0, x_2]$ than in the region defined by $[-x_1, 0]$.

Now consider Fig. 3-6, which shows a particle in a well containing an asymmetric meniscus. Again, P_0 represents the pressure at y_0, P_1 the pressure at y_1, and P_2 the pressure at y_2. Although P_0 is now determined by $y_0 - y_p$ instead of $y_0 - 0$, it is still true that $P_2 < P_1 < P_0$. Therefore, Eqn. 3.34 remains valid.

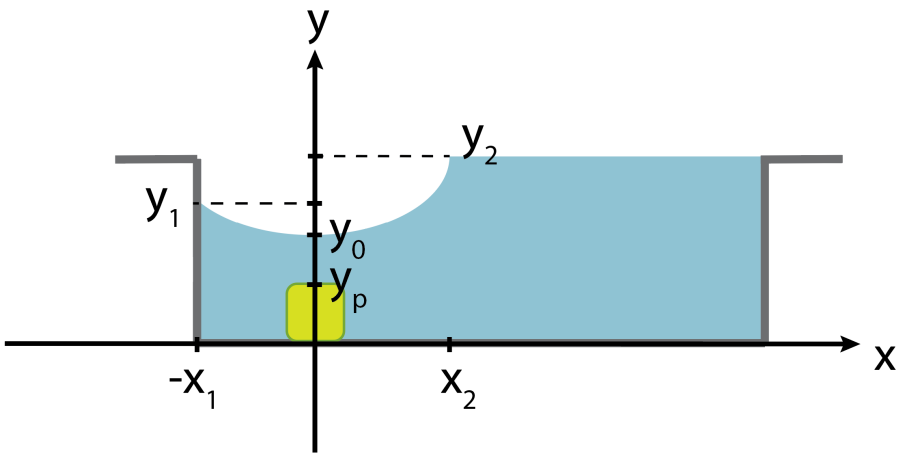

Figure 3-6. Cross-section of well with asymmetric meniscus that contains a particle at $x = 0$.

The pressure gradient produces a force density given by

$$\vec{f} = -\vec{\nabla} P \tag{3.35}$$

The magnitude of the force can be estimated by integrating the force density over volume

$$|\vec{F}| = \iiint_V |\vec{f}| dV \tag{3.36}$$

Given that $|\nabla P_{x_1}| < |\nabla P_{x_2}|$ and $x_2 \approx x_1$ (which means the integration volumes on either side are approximately equal), $|\vec{F}_1| < |\vec{F}_2|$. This means that force on the right side of the well exceeds the force on the left side of the well. From Eqn. 3.35, the direction of the force is opposite to that of the pressure gradient. Since the pressure gradient points in the direction of greatest ascent (i.e. from low pressure to high pressure), the force points from the high pressure region to low pressure region. Therefore, if the force is of sufficient magnitude, it should drive a particle from $x = 0$ (the meniscus minimum) into the region of the well that contains the greatest amount of solvent.

B Work performed

To determine whether the pressure gradient force is of sufficient magnitude to drive a particle within a well, the work done by this force should exceed the randomizing effects of thermal motion. To estimate the work done, consider Fig. 3-7, which shows the cross-section of a well where the depth is varied. This well serves as a first-order approximation to a spherical meniscus, provided that d is small. Let P_0 represent the pressure at (x_0, y_2) and P_1 the pressure at (x_1, y_2). We want to find the work done by the pressure gradient force by moving a small particle (not shown in figure) from (x_0, y_1) to (x_1, y_0).

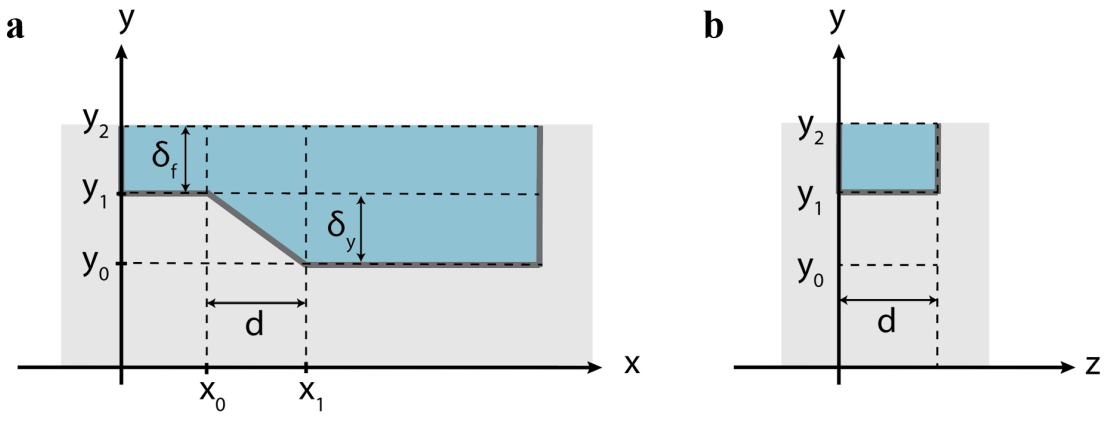

Figure 3-7. Well where depth is locally varied from δ_f to $\delta_f + \delta_y$.
(a) Cross-section at $z = 0$. (b) Cross-section at $x = 0$.

The gradient of pressure is given by

$$\nabla P_x = \frac{P_1 - P_0}{d} \tag{3.37}$$

This pressure can be converted to force using Eqns. 3.35 and 3.36. The well is assumed to have thickness d, so the volume over which the force is applied is approximated by

$$V = \frac{1}{2}\delta_y d^2 \tag{3.38}$$

Combining Eqns. 3.35, 3.36, and 3.38, the magnitude of the force applied is

$$|\vec{F}| = |\frac{P_0 - P_1}{d}|\frac{1}{2}\delta_y d^2 = \frac{1}{2}|P_0 - P_1|\delta_y d \tag{3.39}$$

From Eqn. 3.28,

$$P_0 = P_{bulk} + \frac{A}{6\pi\delta_f^3} \tag{3.40}$$

$$P_1 = P_{bulk} + \frac{A}{6\pi(\delta_f + \delta_y)^3} \tag{3.41}$$

where P_{bulk} is pressure in bulk liquid. We have

$$P_0 - P_1 = \frac{A}{6\pi\delta_f^3} - \frac{A}{6\pi(\delta_f + \delta_y)^3} = \frac{A}{6\pi}\left(\frac{1}{\delta_f^3} - \frac{1}{(\delta_f + \delta_y)^3}\right) \tag{3.42}$$

Using Eqn. 3.39 and 3.42, the work done, defined by $W = Fd$, is therefore found to be

$$W = \frac{A}{12\pi}\frac{(\delta_f + \delta_y)^3 - \delta_f^3}{(\delta_f + \delta_y)^3\delta_f^3}\delta_y d^2 \tag{3.43}$$

As expected, if $\delta_y = 0$, no pressure gradient exists, so $W = 0$. Eqn. 3.43 can be applied to estimate the work performed by a solvent pressure gradient in an SiO_2 well. The Hamaker constant A is determined via an expression provided by Israelachvili [21], namely

$$A = A_{ls} \approx \sqrt{A_{ll}A_{ss}} \tag{3.44}$$

Here, A_{ll} and A_{ss} are the Hamaker constants for identical media interacting in a

vacuum at room temperature. The Hamaker constant for the solvent (dimethyl sulfoxide, DMSO), is $A_{ll} = 6.72 * 10^{-20}$J [22]. The Hamaker constant for the solid (SiO_2) is $A_{ss} = 6.5 * 10^{-20}$J [21]. Fig. 3-8 shows the normalized work with respect to

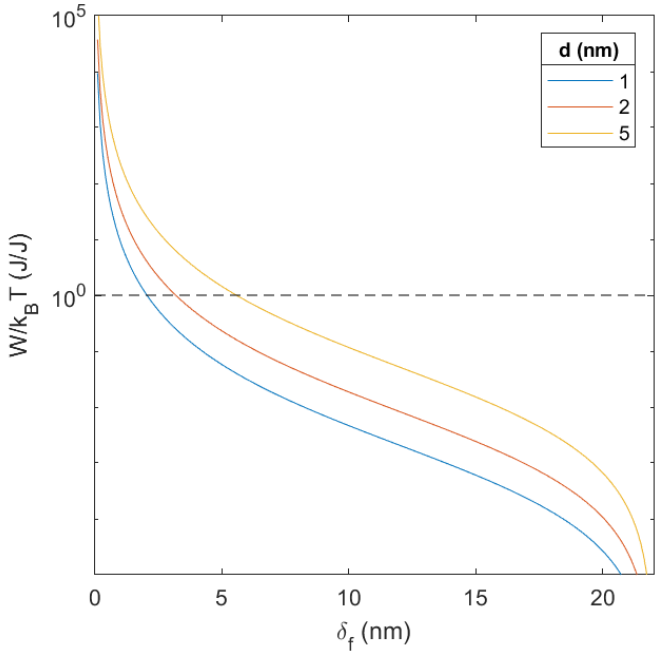

Figure 3-8. Work done by pressure gradient force, normalized by k_BT, for DMSO in a 22 nm tall SiO_2 well. The line at $W/k_BT = 1$ is provided as a visual aid.

δ_f, the local change in z, for various d, the distance over which the force is applied. δ_f sets the maximum pressure possible, so at smaller δ_f, the system does more work. Since the pressure gradient force performs sufficient work to overcome thermal fluctuations when $\delta_f \leq$ 5nm, this plot provides a lower limit for how deep (i.e. $\delta_f + \delta_y$) a meniscus must propagate into the well for the pressure gradient force to take effect.[1]

3.2.2 Asymmetric meniscus

We will now demonstrate how asymmetric menisci can be formed by varying well geometry.

[1]It should be noted that this result is merely an approximation, as more precise result would take into account the liquid-solid interactions between the nucleating particle and DMSO.

Table 3.1. Critical contact angles for various well geometries.

Well geometry	θ_{c_1} (degrees)	θ_{c_2} (degrees)
Square	45	45
Equilateral (60,60,60) triangle	60	60
Isosceles (44,68,68) triangle	56	68
Isosceles (20,80,80) triangle	50	80

A Critical contact angles

First, we compute the critical contact angles for various well geometries using Eqn. 3.5. These results are summarized in Table 3.1. Table 3.1 suggests various conditions for existence of the arc meniscus in an isosceles triangular well. When $0 \leq \theta \leq \theta_{c_1}$, the AM exists both for the larger and smaller corner angles of the triangular well. When $\theta_{c_1} \leq \theta \leq \theta_{c_2}$ the AM disappears from the larger corner angle, and exists only in the smaller corner angle. Finally, when $\theta_{c_2} \leq \theta \leq \frac{\pi}{2}$ the AM ceases to exist in all corner angles. The conditions can be visualized in Fig. 3-9.

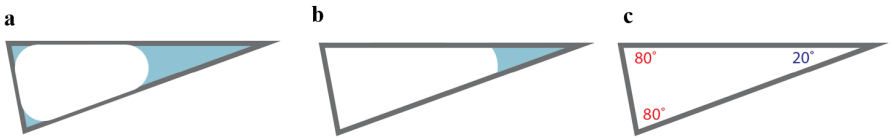

Figure 3-9. Top view of (20,80,80) triangular well showing existence or absence of AM as a function of contact angle. (a) $0 \leq \theta \leq \theta_{c_1}$ (b) $\theta_{c_1} \leq \theta \leq \theta_{c_2}$ (c) $\theta_{c_2} \leq \theta \leq \frac{\pi}{2}$

B Arc meniscus area

The areas of the AM for triangular or square wells can be analytically computed using Fig. 3-10, where r is the radius of the AM and is computed using the expressions of Section C.2.

B.1 Triangular well Using Fig. 3-10a, we see

$$\phi = \frac{\pi}{2} - \frac{\alpha}{2} - \theta \tag{3.45}$$

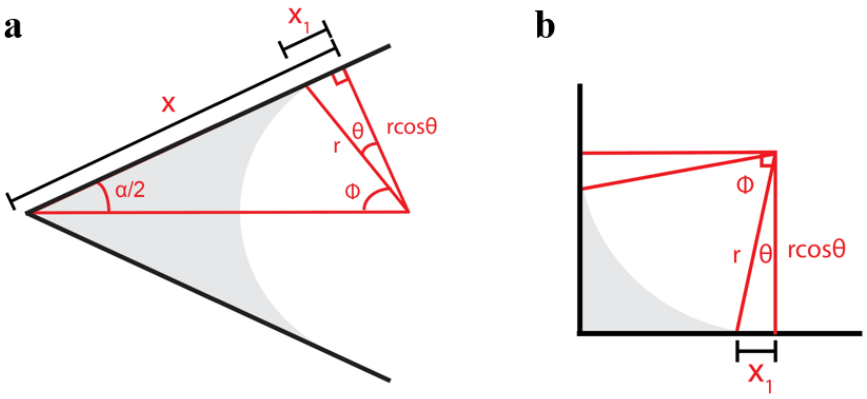

Figure 3-10. Schematics for computing the area occupied by the AM in the single corner of (a) triangular or (b) square well.

$$x_1 = r\cos\theta\tan\theta \tag{3.46}$$

$$x = \frac{r\cos\theta}{\tan\frac{\alpha}{2}} \tag{3.47}$$

The area subtended by ϕ is given by

$$A_1 = \pi r^2\frac{\phi}{2\pi} \tag{3.48}$$

The triangle with base x_1 has area

$$A_2 = \frac{1}{2}x_1 r\cos\theta \tag{3.49}$$

The triangle with base x has area

$$A_3 = \frac{1}{2}xr\cos\theta \tag{3.50}$$

Combining Eqns. 3.48, 3.49, and 3.50, the area of the AM in any given corner of a triangular well is

$$A_{AM} = 2(A_3 - A_2 - A_1) \tag{3.51}$$

$$A_{AM} = r^2\left(\cos^2\theta\left(\frac{1}{\tan\frac{\alpha}{2}} - \tan\theta\right) - \frac{\pi - \alpha - 2\theta}{2}\right) \tag{3.52}$$

When $\theta = 0$, Eqn. 3.52 simplifies to

$$A_{AM} = r^2 \left(\cot \frac{\alpha}{2} - \frac{\pi - \alpha}{2} \right) \tag{3.53}$$

which agrees with the result presented in [23].

B.2 Square well Using Fig. 3-10b, we see

$$\phi = \frac{\pi}{2} - 2\theta \tag{3.54}$$

$$x_1 = r \cos\theta \tan\theta \tag{3.55}$$

The area subtended by ϕ is given by

$$A_1 = \pi r^2 \frac{\phi}{2\pi} \tag{3.56}$$

The area of each triangle is

$$A_2 = \frac{1}{2} x_1 r \cos\theta \tag{3.57}$$

The area of the red square is

$$A_3 = r^2 \cos^2\theta \tag{3.58}$$

Combining Eqns. 3.56, 3.57, and 3.58, the area of the AM in any corner of a square well is

$$A_{AM} = A_3 - 2A_2 - A_1 \tag{3.59}$$

$$A_{AM} = r^2 \left(\cos^2\theta \left(1 - \tan\theta \right) - \frac{\pi}{4} + \theta \right) \tag{3.60}$$

B.3 AM area as function of contact angle The analytical expressions of Sec. B.1 and B.2 can be used to plot AM area as a function of contact angle. Fig. 3-11 shows AM area for each angle of two differently-shaped isosceles triangles of equivalent total area ($A = 2.25 * 10^4$ nm^2). For both triangles, the area of the AM is greater for the smaller angle (20 or 44 degrees) than for the larger angle (80 or 68 degrees). Further, the area of the AM for each angle goes to zero at the critical contact angles

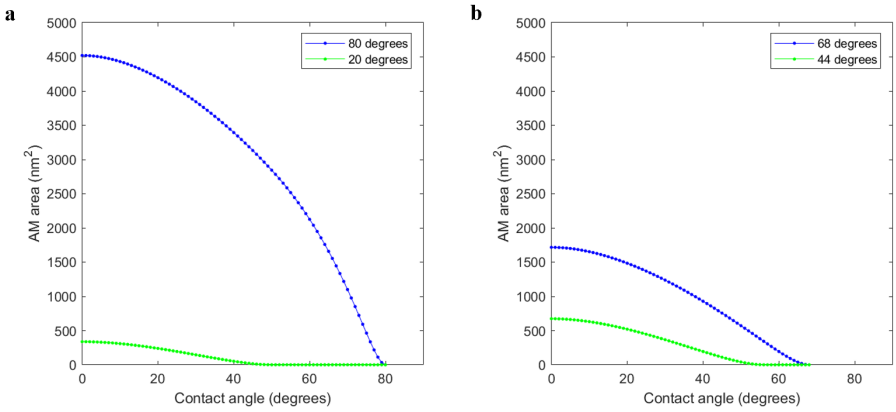

Figure 3-11. AM area for isosceles triangles of total area $A = (2.25 * 10^4 \text{ nm}^2)$. (a) (20,80,80) triangle (b) (44,68,68) triangle

displayed in Table 3.1 (i.e. θ_{c_1} for the larger triangle angle and θ_{c_2} for the smaller triangle angle). Since the two triangles have the same total area, the AM areas for the two triangles can be directly compared. We see that AM area for the small angle of the (20,80,80) triangle is significantly greater for all contact angles than the AM area of the small angle of the (44,68,68) triangle. This means that the small angle of the (20,80,80) triangle holds more solvent during drainage than that of the (44,68,68) triangle. Fig. 3-12 compares the AM area of the smallest angle for 4 different well geometries (i.e. 20° for the (20,80,80) triangle, 44° for the (44,68,68) triangle, 60° for the (60,60,60) triangle, and 90° for the square). We see that as the smallest angle decreases, the area of the AM contained within the smallest angle increases. This suggests that slit-shaped geometries hold more solvent during drainage than non-slit shaped geometries.

C 3D models of menisci during drainage

The shape of the meniscus during drainage can be approximated using the AM radii for each geometry. Fig. 3-13 shows the shape of meniscus for a 22 nm tall well with sidewall contact angle $\theta = 50°$. The main terminal meniscus (MTM) takes on a spherical shape. During evaporation, the MTM has a radius governed by the pinning points of the well. If the corner angle contains an AM, then the MTM pins at the edge of the AM [24]. If the corner angle does not contain an AM, then the MTM

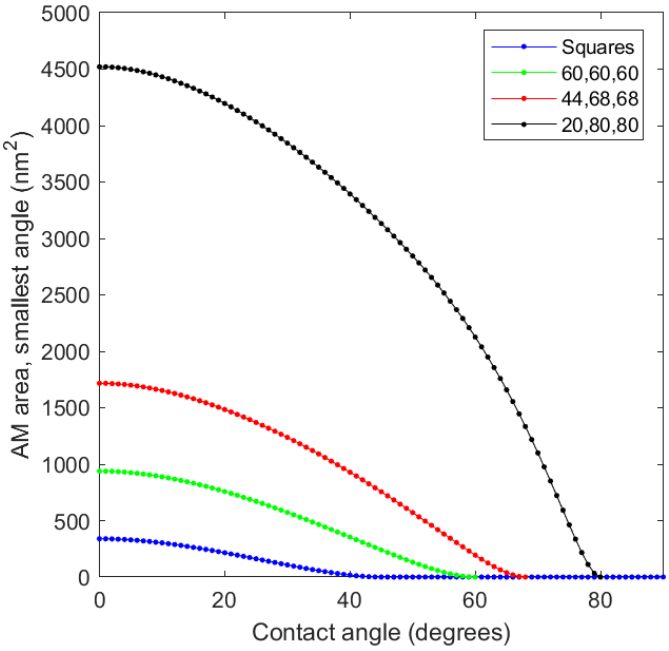

Figure 3-12. AM area for smallest angle for 4 different well geometries

pins at the corner [25, 26]. In this figure, the MTM is shown as a spherical cap whose height is 80% that of the well (i.e. $h_{cap} = 0.8h_{well} = 17.6\,\text{nm}$). From Table 3.1 and Fig. 3-12, when $\theta = 50°$, $\theta > \theta_{c,square}$, so the corners of square well do not contain the AM. This is reflected in Fig. 3-12a, which shows the MTM pinned at the corners of the square well. For the (60,60,60) and (44,68,68) triangles (Fig. 3-12b,c), $\theta < \theta_{c_1}$, so the AM is contained within all three corners. The MTM is therefore pinned at the edge of the AMs. Finally, for the (20,80,80) triangle, (Fig. 3-12d), $\theta_{c_1} \leq \theta \leq \theta_{c_2}$, so the AM is only contained within the small corner angle.

3.2.3 Force balance for asymmetric menisci

From Fig. 3-13, it is clear that the MTM shape is affected by well geometry. To better understand how in asymmetric wells the MTM takes on an asymmetrical shape, consider Fig. 3-14, which shows the meniscus at the plane given by the angle bisector of the smallest angle. At this plane, the meniscus resembles Fig. 3-5. However, since this view is taken by cutting the well, we can see that the meniscus pins at back

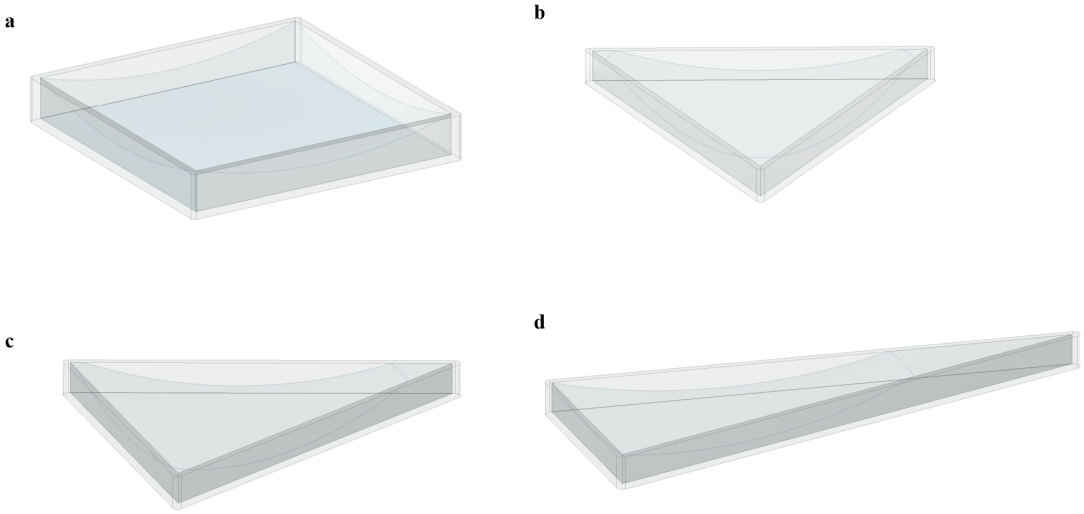

Figure 3-13. Meniscus during drainage for 50 degree sidewall contact angle in various well geometries of equivalent volume. (a) Square. (b) Equilateral (60,60,60) triangle. (c) (44,68,68) triangle. (d) (20,80,80) triangle.

corner of the triangle. To understand how this affects the balances of forces in the triangular well, consider the force diagram in Fig. 3-15. The orientation of the axes is chosen so as to be consistent with the axes of Fig. 3-5. In the diagram, an arrow is drawn for each direction that the meniscus has height $y_2 - y_0$ (from Fig. 3-5). Since the triangle is isosceles, the z-components of all forces cancel each other out. The summation of the x-components of the forces directed to the right clearly exceeds the summation of the x-components of the two forces directed to the left. The net force is therefore directed into the corner with the AM.

The relationship between AM area and contact angle suggests that contact angle should also affect the net force. Consider Fig. 3-16, which shows asymmetric menisci for two different AM areas. Let P_0 represent the pressure at y_0 and P_2 the pressure at y_2. The pressure gradients for the menisci given by AM_1 and AM_2 can be computed as follows:

$$\nabla P_{AM_1} = \frac{P_2 - P_0}{d_1} \tag{3.61}$$

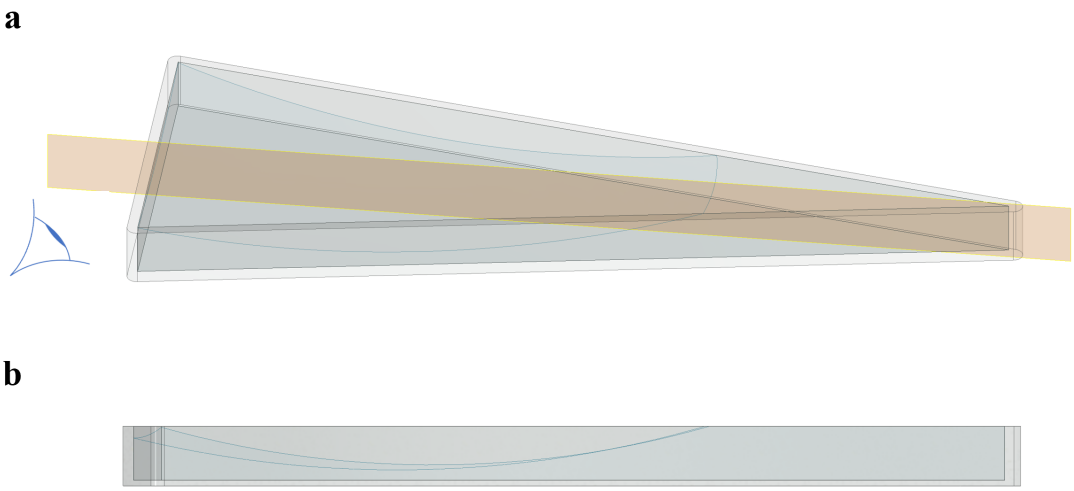

Figure 3-14. Asymmetric meniscus in (20,80,80) well. (a) 3D model, with plane of cut identified in yellow (b) Meniscus viewed at plane of cut, at the viewing position identified by the eye.

$$\nabla P_{AM_2} = \frac{P_2 - P_0}{d_2} \tag{3.62}$$

Since $d_2 > d_1$, the ratio of the magnitudes of the two pressure gradients is

$$\frac{|\nabla P_{AM_1}|}{|\nabla P_{AM_2}|} = \frac{d_2}{d_1} > 1 \tag{3.63}$$

This means that the more solvent a corner angle contains during drainage (i.e. the higher the AM area), the higher the expected pressure gradient. AM area is inversely related to contact angle θ. Here, $AM_1 > AM_2$, so $\theta_1 < \theta_2$. Therefore, we expect that the pressure gradient, and resulting force, to be higher for lower θ. This result suggests that lower contact angles for the preferred geometry should demonstrate improved particle positioning compared to higher contact angles, since the net force should be stronger for lower contact angles.

3.3 Discussion

The results demonstrate that the magnitude and the direction of the pressure gradient force is sufficient to drive a particle from the meniscus minimum into the corner

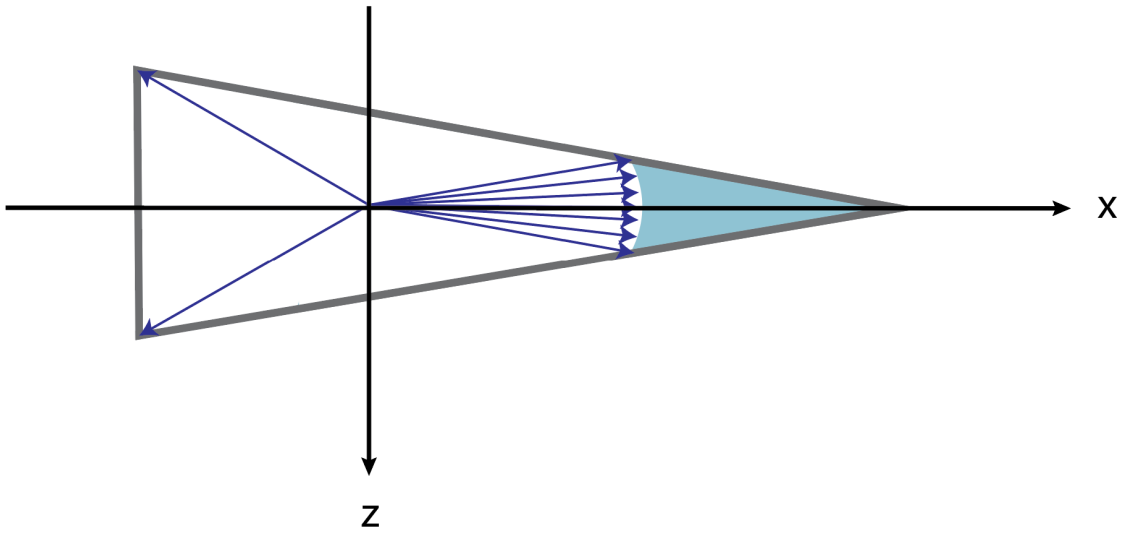

Figure 3-15. Force diagram for (20,80,80) well. Force is directed from high pressure region to low pressure region.

containing the greatest amount of solvent. These results therefore suggest a method for positioning perovskite nanocrystals within wells. The method can be summarized in the following points:

1. A lithographically-patterned well is filled with perovskite precursor solution.
2. During drainage (in this case, evaporative), the MTM propagates into the well. The shape of the MTM is controlled by the AM in each corner, which in turn are controlled by well geometry and sidewall contact angle (Fig. 3-12).
3. When the solubility limit of the precursor solution is locally exceeded, a nanocrystal nucleates. The meniscus minimum contains the least volume of solvent, so the concentration is at a local maximum there. The nanocrystal therefore nucleates at the meniscus minimum.
4. When the MTM propagates sufficiently deep into the well (Fig. 3-8), the disjoining pressure begins to take effect.
5. Asymmetry in the MTM yields a pressure gradient, and resultant force. The net force is directed into the corner of the well containing the greatest amount

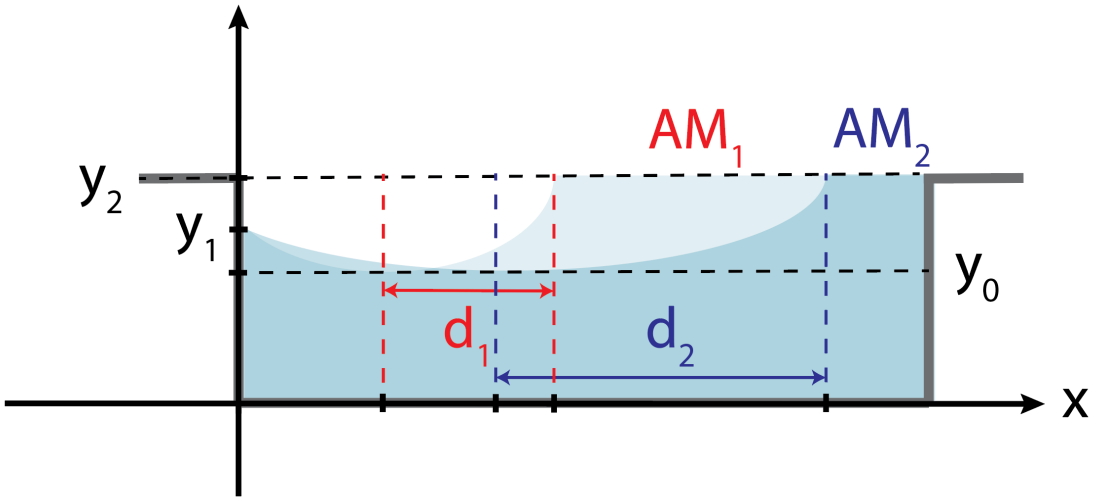

Figure 3-16. Asymmetric meniscus for two different AM areas.

of solvent (Figs. 3-6 and 3-15).

6. The preferred geometry is one that during drainage, contains significantly more solvent in one corner than in other corners. The preferred geometry is therefore a slit-shaped triangle (Fig. 3-13).

7. Higher AM areas, which results from lower contact angles, yield greater pressure gradients. Improved positioning accuracy is therefore expected at lower contact angles for the preferred geometry.

Experimental verification for this method will be presented in Chapter 4.

Chapter 4

On-site growth of perovskite nanocrystals

4.1 Introduction

This chapter will provide experimental demonstration of on-site growth of perovskite nanocrystals with high-positional accuracy.

4.2 Methods

4.2.1 Chemicals

Lead (II) bromide (Sigma-Aldrich, 99.999%), cesium bromide (Sigma-Aldrich, 99.999%), trichloro(1H,1H,2H,2H-perfluorooctyl)silane (PFTS, Sigma-Aldrich, 97%), 1H,1H,2H,2H-perfluorodecyltriethoxysilane (PFDTES, Sigma-Aldrich, 97%), polystyrene (Sigma-Aldrich, average MW 35k), dimethyl sulfoxide (Sigma-Alrich, anhydrous, 99.9%), toluene (Sigma-Aldrich, anhydrous, 99.8%), ethanol (Sigma-Aldrich, anhydrous, 99.5%), methyl isobutyl ketone (MIBK, Dow Corning), hydrogen silsesquioxane e-beam resist (HSQ, Dow Corning, XR-1541) were used as received.

4.2.2 Solution preparation

To prepare the $CsPbBr_3$ precursor solution, $PbBr_2$ powder was first dissolved in anhydrous DMSO to form a 0.45 M solution. $PbBr_2$ solution was added to a vial containing CsBr powder to produce a 0.45 M $CsPbBr_3$ solution. (The solubility of CsBr increases in presence of $PbBr_2$, so this method ensures that CsBr can be fully dissolved.) The $CsPbBr_3$ solution was stirred overnight. Polymer encapsulating solution was prepared by dissolving 3 wt% polystyrene in toluene, then filtering the solution with a 1 μm PTFE filter. All solutions were prepared in a nitrogen-filled glovebox.

4.2.3 Template fabrication

To prepare the surface-functionalized topographical templates, substrates (silicon ("Si"), or silicon/ silicon dioxide with 1 μm oxide thickness ("SiO_2")) were washed sequentially with acetone under sonication (twice for 2 min each) and boiling isopropanol (twice for 2 min each). Samples were then treated by either 3 min of oxygen plasma treatment. HSQ was spin-coated onto substrates after plasma treatment.

For all substrates, HSQ (1 vol% in MIBK) was spin-coated at 1500 rpm under 3,000 rpm/s acceleration for 90 s, yielding a thickness of 22 nm, as measured by ellipsometry and atomic force microscopy. Samples were exposed at a base dose of 11,000 $\mu J/cm^2$ using an Elionix FS-125 electron-beam lithography system operating at 2 nA beam current and 125 keV accelerating voltage, using a 1 nm pixel size.

Immediately after e-beam exposure, vapor phase growth of molecules (PFTS or PFDTES) was performed by leaving samples under vacuum in a desiccator containing 30 μL of PFTS for 10 min or 30 μL of PFDTES and 90 μL of deionized (DI) water for 6 hours. After molecular growth, samples were developed in salty developer solution (1 wt% NaOH and 4 wt% NaCl dissolved in DI) for 1 min, [27] then rinsed with gentle stirring in DI three times for 2 min each, using fresh DI for each rinse. After DI rinsing, samples were blown-dry with nitrogen gas, rinsed with

gentle stirring in isopropanol two times for 2 min each, using fresh isopropanol for each rinse, then blown-dry again with nitrogen. To ensure the molecular layer remains consistent across samples, the volumes of development and rinsing solutions were standardized (10 mL per vial for our 1 cm by 1 cm or 0.5 in by 0.5 in samples), and fresh development and rinsing solutions were used for each sample. After development, the same molecule (PFTS or PTDTES) was briefly deposited again by leaving the samples under vacuum in a desiccator for 5 s for PFTS, or between 10-40 min for PTDTES. After this, samples were rinsed in isopropanol for 5 s with gentle stirring, and DMSO contact angle was measured (see Sec. 4.2.5).

4.2.4 Growth of particles in templates

Particle growth was performed in a nitrogen-filled glove box held at 5 mbar above standard pressure immediately after template fabrication. Precursor solution was deposited by spin-coating 15 μL of precursor solution at 1000 rpm for 30 s, using 1000 rpm/s acceleration. After deposition, samples were allowed to dry under ambient temperature in the glove box with circulation off for 30 min, then annealed at 80 °C for 1 min each. For samples used in single-particle spectroscopy measurements, 100 μL of polymer encapsulating solution was spun at 5000 rpm for 60 s under 5000 rpm/s acceleration after annealing.

4.2.5 Contact angle measurements

Static contact angles were determined by drop-casting 0.5 μL of DMSO on a substrate, and imaging the droplet profile. Images were processed using the low bond axisymmetric drop shape analysis (LB-ADSA) plug-in of open-source software ImageJ [28, 29]. Contact angles were measured in ambient air immediately after molecular growth.

4.2.6 Optical measurements

Fluorescence images were acquired using a Nikon Eclipse LV100 microscope with an attached CMOS sensor camera (AmScope, MU1203-FL). The sample was illuminated by a 100 W halogen lamp through a filter cube consisting of a 475/35 nm excitation filter, 530/43 nm emission filter, and 499 nm edge dichroic mirror (Semrock, BrightLines, FITC-A-Basic-NTE). Images were obtained using a 50X, 0.80 NA objective (Nikon) under 2000 ms of integration time.

Fluorescence measurements were performed using a custom-built confocal microscope. Samples were excited by a 405 nm pulsed laser (PicoQuant, LDH-P-C-405, $<$90 ps pulse duration), which was focused by a 100X, 0.85 NA objective (Nikon) to yield a $\sim$ 640 nm diameter ($1/e^2$) spot size. Laser excitation was directed onto the sample through 405nm dichroic filter with 423 nm cut-on wavelength (Chroma, zt405rdc TIRF). Sample fluorescence was collected using the same objective and dichroic. Samples were excited at 57 W/cm^2 and 10 MHz repetition rate. Particle spectra were acquired by first confocally mapping the region of interest (i.e. an array of particles) to identify the locations of particles, then collecting spectra from individual points on the array. Mapping was performed by scanning the sample using a piezoelectric scanning stage (Physik Instrumente, P-733.3CL). Emitted light was passed through a 450 nm long-pass filter (ThorLabs, FEL0450) to remove residual excitation light. Photons were detected using a single-photon detecting avalanche photodiode (Micro Photon Devices, PD-050-00E) connected to a single-photon counting module (PicoQuant, PicoHarp 300) and counted using commercial software (PicoQuant, SymphoTime 64). Fluorescence spectra were collected using a monochromator (Princeton Instruments, SP2300) and a thermoelectrically-cooled CCD (Princeton Instruments, PIXIS 100). Spectra were obtained using 5000 ms of integration time.

4.2.7 Structural characterization

A Lateral size and positioning in wells

Templates were imaged using the in-lens detector of a Zeiss Gemini 450 scanning electron microscope (SEM). Images were acquired at a working distance of 4.0-4.3 mm, under 1.00 kV accelerating voltage, 1 nA beam current, and 24X-100X magnification. SEM images were processed to determine the size and position of particles in wells using custom code written in MATLAB, as is summarized below:

- ***Particle size*** The lateral size of particles was determined using high-magnification images (i.e. 60X-100X, depending on well size). Particles were distinguished from background by performing morphological operations (dilation, filling, and erosion) on flattened and binarized SEM images, and identifying the connected regions. The length (/width) of a particle was defined as the major (/minor) axis length of a given connected region. Measurements were converted from pixels to nanometers using the image scale bar.

- ***Particle positioning*** The locations of particles in each well were determined using lower-magnification images (40X), which provided a larger field of view and hence higher throughput. The location of each particle (x_i, y_i) in a well was defined with respect of the centroid of the well, which was set as (0,0). Well centroids were identified by performing morphological operations (dilation, filling, and erosion) on flattened and binarized SEM images, then finding the centroid of each resultant connected region. Particle centroids were similarly identified.

For both particle size and particle positioning, measurements were converted from pixels to nanometers using the image scale bar. If a well contained multiple nucleations, the data was appropriately tagged for data analysis.

B Height

Particle height was characterized using an atomic force microscope (Asylum Research, Cypher S) operating in AC mode, with a 160AC-NA cantilever. Scans were acquired at 1 Hz. Second-order flattening was performed on regions surrounding each well to remove offset, slope, and bow. Flattening was performed via commercial software (Asylum Research, IgorPro). Line traces of flattened images were taken using MATLAB. Particle height was defined as the maximum height of a particle from the bottom of the well.

C Elemental analysis

Energy-dispersive x-ray analysis (EDS) was performed using a Oxford AZtec 100 EDS detector attached to a Zeiss Gemini 450 SEM. Images were taken at a working distance of 8.5 mm, under 10.00 kV accelerating voltage[1] and 1 nA beam current. Maps were acquired using the AZtecLive software, and exported using a binning factor of 2 and smoothing level of 3.

4.2.8 Data analysis

A Positional accuracy

The positional accuracy of each well geometry, i.e. the expected distance of particles from a chosen reference point, was calculated using the following definition:

$$A = \frac{\sum_{i=1}^{n} \sqrt{(x_i - x_c)^2 + (y_i - y_c)^2}}{n} \tag{4.1}$$

Here, (x_i, y_i) represents the coordinates of particle i, (x_c, y_c) represents the coordinates of the reference point, and n represents the total number of particles. Since the ideal well geometry would yield all particles located within one particular corner, cluster analysis was performed on the list of particle coordinates to identify the cluster (i.e.

[1]To limit material degradation during detection, the minimum voltage needed to detect all elements was used. For Pb and Br, the minimum accelerating voltage is 5.00 kV, whereas for Cs, the minimum voltage is 10.00 kV [30].

well corner) containing the greatest fraction of particles. The center of this cluster was then set as (x_c, y_c). In this definition, if all particles were located in the cluster having center (x_c, y_c), then accuracy $A \to 0$. A low value of A therefore indicates that a given well geometry yields high positional accuracy.

Positional accuracy for various well geometries was computed using data from at least 90 wells per geometry.

B Single particle-well fraction

Single particle-well fraction is calculated using the following definition:

$$\text{SPWF} = \frac{W_1}{W_1 + W_2 + W_3} \tag{4.2}$$

where W_i represents the number of wells containing i particles per well.

C Particle volumes

The mean volume of particles contained with a given well size was calculated using

$$V = \mathrm{E}\left[\prod_{i=1}^{3} X_i\right] = \prod_{i=1}^{3} \mathrm{E}[X_i] \tag{4.3}$$

where $\mathrm{E}[X_i]$ was the mean length in nm of the i-th particle dimension, as characterized by SEM or AFM. This expression assumes mutual independence for $X_1 ... X_n$, so SEMs and AFMs did not need to be correlated.

The variance in volume, i.e. the variance for the product of mutually independent random variables, was calculated using

$$\mathrm{Var}(X_1 X_2 X_3) = \prod_{i=1}^{3}(\mathrm{Var}(X_i) + (\mathrm{E}[X_i])^2) - \prod_{i=1}^{3}(\mathrm{E}[X_i])^2 \tag{4.4}$$

If a well contained two particles, total particle volume was calculated according to

$$V_{tot} = \sum_{i=1}^{2} V_i \tag{4.5}$$

The variance in volume for a well containing two particles was computed using

$$\mathrm{Var}(V_{tot}) = \mathrm{Var}(V_1 + V_2) = \mathrm{Var}(V_1) + \mathrm{Var}(V_2) + 2\mathrm{Cov}(V_1, V_2) \tag{4.6}$$

4.3 Results

4.3.1 On-site growth with topographical templates

In Ch. 2, we noted that topographical templates can be utilized to locally confine perovskite precursor solution for on-site growth of perovskites. With these templates, positional accuracy is first and foremost governed by the size of the lithographically-patterned well. To demonstrate high-positional accuracy growth, we therefore first explored whether a topographical template patterned via electron-beam lithography (EBL) could enable growth of perovskite nanocrystals.

For the template to selectively confine perovskite precursor solution, the template must consist of wetting wells bored into a non-wetting surface. Fig. 4-1a demonstrates how an asymmetrically-wetting template can be fabricated using EBL. First, HSQ, a negative e-beam resist, is spun to the desired thickness on a hydrophilized substrate. HSQ was chosen as the resist since it (i) enables high-resolution patterning [27] and (ii) transforms into an oxide of silicon upon exposure that does not dissolve in organic solvents (in which perovskite precursor solutions are prepared). Following exposure, molecules (PFTS or PFDTES) are grown on HSQ in vapor-phase. PFTS grows rapidly, allowing for a $\sim 70^\circ$ contact angle with DMSO to be achieved in 10 min (Fig. 4-1b). After molecule growth, the HSQ is developed, exposing the hydrophilic interior of the well. The contact angle of the well interior is then further tuned via a second, shorter molecular growth step.

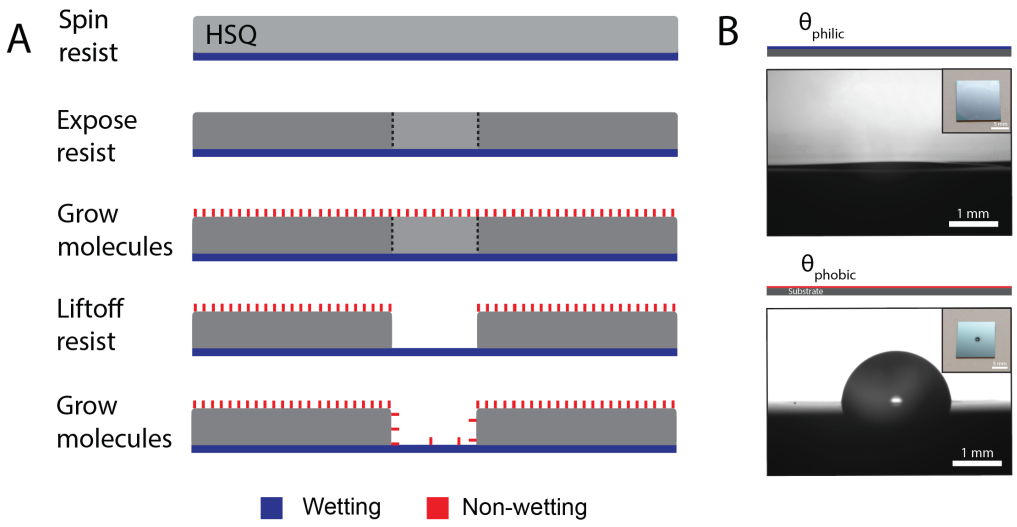

Figure 4-1. (a) Scheme for fabricating asymmetrically-wetting template (not drawn to scale). (b) DMSO droplets on an SiO_2/Si substrate treated by O_2-plasma (top) or PFTS (bottom). Insets show top view of droplet.

Fig. 4-2 details the full fabrication flow. Precursor solution is first drop-cast onto the template. The excess solution is then removed from the template via spin-coating. Finally, the samples are allowed to dry to allow nanocrystal nucleation and growth, and annealing is performed to remove any residual solvent from the crystal. To ensure material quality, nanocrystal growth is performed in an inert environment.

Fig. 4-3 shows that asymmetrically-wetting templates can be applied for large-area, on-site growth of nanocrystals from precursors of $CsPbBr_3$. The fluorescence image shows that the particles display the green emission expected of $CsPbBr_3$.

The chemical composition of nanocrystals was further confirmed via energy dispersive x-ray spectroscopy (EDS) and fluorescence spectroscopy, as shown in Fig. 4-4. The fluorescence spectrum shows that the nanocrystal displays an emission peak at 508 nm, corresponding to a bandgap of 2.44 eV. While this peak corresponds to green emission, the peak is blue-shifted with respect to that for bulk $CsPbBr_3$. This blue-shift will be discussed in greater detail later.

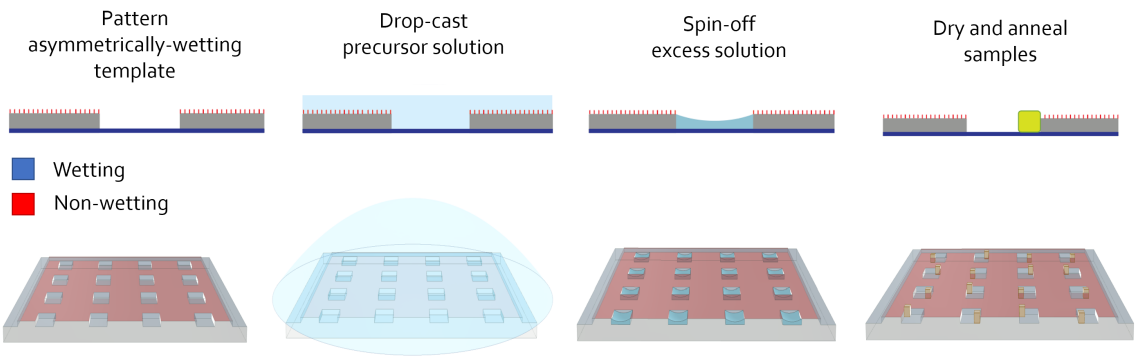

Figure 4-2. Fabrication flow for on-site growth of perovskite nanocrystals.

4.3.2 Well asymmetry for particle positioning

Having demonstrated that the EBL-patterned topographical templates enable on-site growth of nanocrystals, we next sought to explore whether well geometry could be tuned to position nanocrystals within wells (see Ch. 3). To isolate the effect of well geometry on positioning, we designed a template containing wells of the four geometries analyzed in Sec. 3.2.2, which we patterned on a SiO_2/Si substrate. The template was designed such that the area, height, and hence volume of wells was constant for the various geometries. Well height was made constant (22 nm) by containing the geometries within a 30 μm region of the same template. Well area was made constant by appropriately scaling the lateral dimensions of the well patterns. The area was chosen to correspond to that of a square with 150 nm sides; this area also matches the area used for AM computations in Fig. 3-12.

The contact angle of the interiors of wells was also held constant, since all wells of the template experienced the same molecular growth duration. Since both the substrate on which the template was patterned and the interiors of wells were silicon oxide, we expected the contact angle made by DMSO (the solvent our precursor solution was prepared using) on the substrate to match the contact angle made by DMSO with the sidewalls of the wells. We therefore measured the contact angle on the substrate

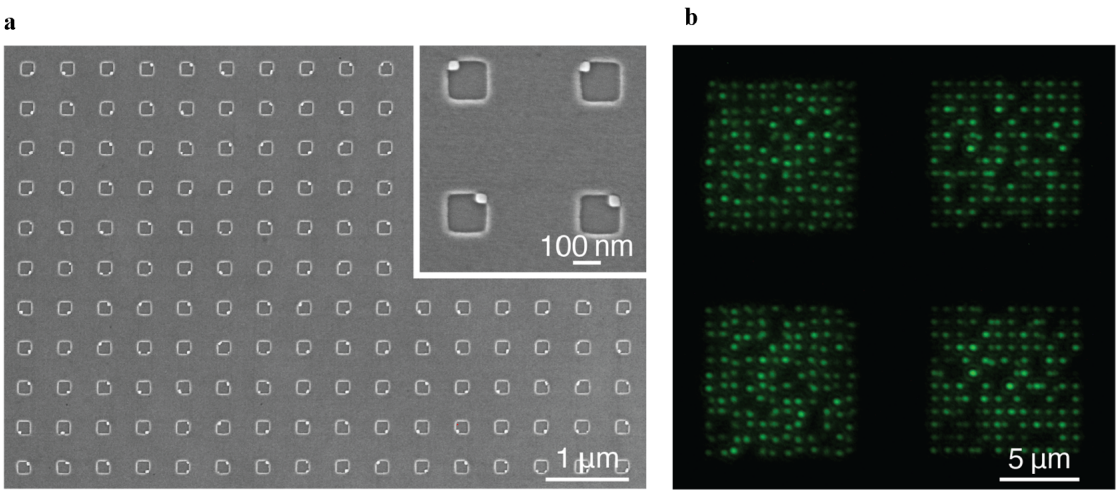

Figure 4-3. (a) SEM micrograph demonstrating large-area growth of $CsPbBr_3$ nanocrystals using asymmetrically wetting template. Inset shows high-magnification view of nanocrystals. (b) Fluorescence image of $CsPbBr_3$ nanocrystal arrays.

immediately before particle growth, and took this value (50°) to be the contact angle of solvent in the wells.

Fig. 4-5 shows how well geometry affects particle positioning. SEM images were analyzed to determine the position of particles with respect to the centroids of their containing wells; the results for particles from >90 wells per geometry are plotted. In these plots, each point corresponds to one particle. The coloration of a point defines whether other particles were contained in the same well as the identified particle. (Red signifies that the particle was the only particle in the well; blue signifies that the particle was one of two particles in the well, and gray signifies that the particle was one of three). To help visualize whether points overlay on another, partially transparent points (with opacity = 60%) are used. A dark region therefore indicates the presence of many closely-located points.

We note that for the two symmetric well geometries (square and (60,60,60) triangle), (i) particles reside in all of the corners of the wells, and (ii) multiple particles are found in many wells. By contrast, for the asymmetric geometries ((44,68,68) and (20,80,80) triangles), particles preferentially locate in the small corner angle. Visual observations

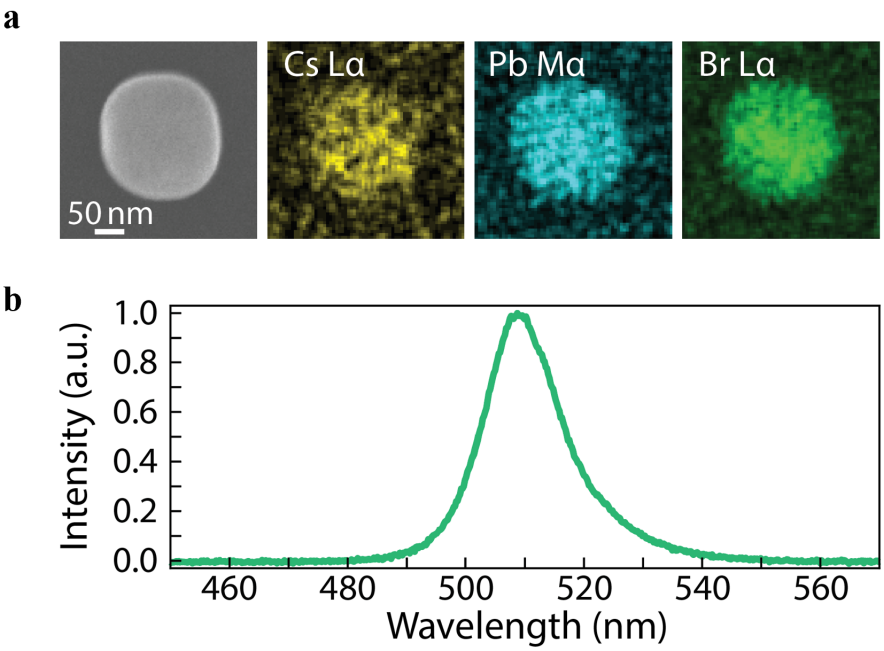

Figure 4-4. (a) SEM image and EDS maps for $CsPbBr_3$ nanocrystal. Substrate is SiO_2/Si. (b) Fluorescence spectrum of a $\sim$ 46nm (lateral size) $CsPbBr_3$ nanocrystal.

are supported by cluster analysis, which suggests that 65% of all particles are located in the 44° angle of the (44,68,68) triangle, and 86% of all particles are located in the 20° angle of the (20,80,80) triangle. For wells displaying only one particle per well, we further find that 95% of particles are located in the 44° angle of the (44,68,68) triangle, and 100% of particles are located in the 20° angle of the (20,80,80) triangle.

To better compare the various well geometries, we compute two figures of merit: positional accuracy and single particle-well fraction. These figures are computed using the definitions expressed in Sec. 4.2.8. The results are shown in Fig. 4-6. As mentioned previously, positional accuracy is defined as mean displacement from a fixed reference (i.e. the corner containing the greatest fraction of particles). A low value for positional accuracy therefore indicates that a given well geometry positions all particles close to the fixed reference. We see that for the symmetric well geometries, positional accuracy is defined by the size of the lithographically-patterned well. From Appendix C, we know that if the distribution of particles

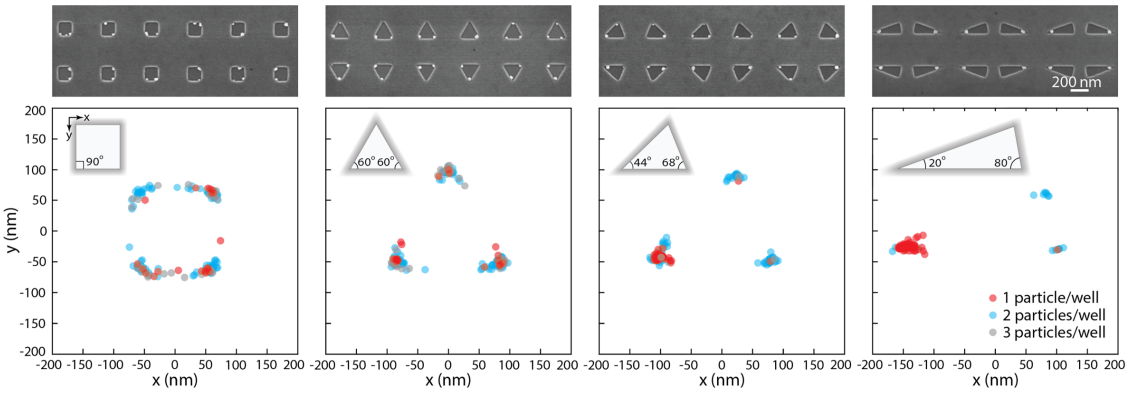

Figure 4-5. Nanocrystal positioning as a function of well geometry. SEM images (top) and population-based analysis of particle positions with respect to well centroid (bottom). From left to right, wells are square, equilateral (60,60,60) triangle, (44,68,68) triangle, or (20,80,80) triangle.

among the corners of the equilateral triangle and square is perfectly uniform, then the ratio of the positional accuracies is $A_{tri}/A_{sq} \approx 1.19$. Here, the experimental results yield a ratio $A_{tri}/A_{sq} = 1.16 \pm 0.075$. The symmetric wells therefore demonstrate the theoretically-predicted positional accuracy. Further, the symmetric wells demonstrate a low single particle-well fraction, meaning that many wells contain multiple particles per well.

Importantly, as wells become more asymmetric, both positional accuracy and single-particle well fraction improve. For the most asymmetric well, positional accuracy is 40.9 ± 7.7 nm and the single-particle well fraction is 0.80. These results suggests that well asymmetry not only enables precise particle positioning, but also reduces the likelihood that multiple particles per well are formed.

4.3.3 Particle size

Having explored how well geometry affects particle positioning, we sought to investigate how well volume, particularly for the optimal well geometry, affects particle size (i.e. volume). To conduct this study, we considered three well volumes: 1X, 1.78X, 2.78X. (Here, "1X" denotes the well volume studied in Sec. 4.3.2.) Since our template fabrication method does not allow for local variation in height, we

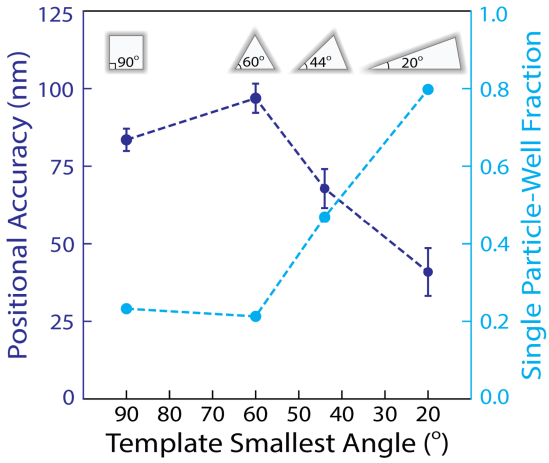

Figure 4-6. Positional accuracy and single particle-well fraction for four well geometries of constant area.

varied well volume by linearly scaling well area while holding well height constant. For each well size, we randomly sampled >30 wells and studied the contained particles via AFM and SEM. Fig. 4-7a shows representative AFM scans and SEM images for wells of various sizes. Both the SEM images and the AFM line traces suggest that particle size increases with increasing well volume. However, as the images suggest, the wells can contain either one or two particles. To determine whether particle volume scales with well volume, we therefore computed the expected total particle volume to be contained within a well of each size.

In our sampling, the 1X wells primarily contained one particle per well, while the 2.78X wells contained two particles per well. However, the 1.78X wells contained either one or two particles in sufficient numbers ($n = 11$ vs $n = 25$, respectively), that the two populations could be independently studied. Fig. 4-7b displays total particle volume as a function of well volume. The figure shows that total particle volume is linearly related to well volume. Importantly, the volumes for the two populations of 1.78X wells (which have well volume 8.8×10^5 nm^3) are statistically indistinguishable, as indicated by the overlapping error bars. This result suggest that wells confine the same volume of precursor solution; varying evaporation dynamics then alter whether one or two particles are formed.

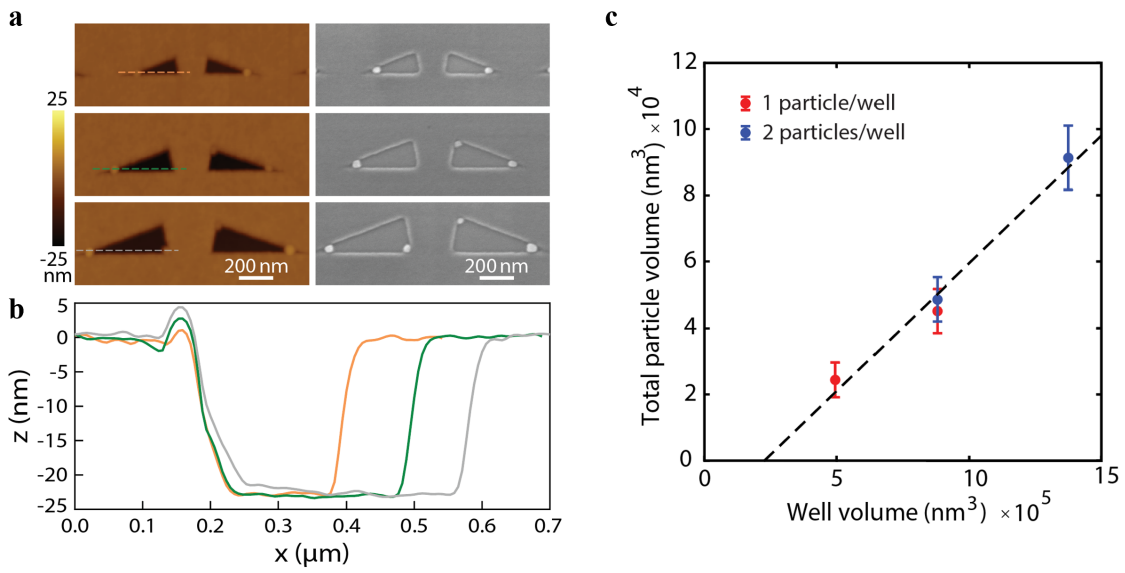

Figure 4-7. (a) Representative AFMs (left) and SEMs (right) for (20,80,80) triangle wells. From top to bottom, volume scaling factor is 1X, 1.78X, 2.78X. "1X" corresponds to well volume studied in Sec. 4.3.2. (b) AFM line traces taken at y positions indicated in "a". (b) Total particle volume vs well volume for (20,80,80) triangle wells.

We further wished to study whether the particles of different sizes exhibited varying optical properties. Fig. 4-8 shows the PL spectra for 30 wells of each well size. We see that that largest wells yield the broadest and most red-shifted spectra. We attribute the spectral broadening to the simultaneous excitation of both particles within the well, since our laser spot size ($\sim$ 640nm) is still larger than the largest dimension of the well. We further note that as the size of well decreases, the degree of broadening also decreases, but only on the red side of the spectrum. Given that the larger particle in the well likely produces redder-emission [12], we speculate the one-sided spectral narrowing results from the larger particle decreasing to a greater degree than the smaller particle with decreasing well size.

4.3.4 Effect of contact angle

In the work discussed so far, contact angle was held constant. However, we hypothesized that contact angle should also affect particle positioning. Fig. 4-9

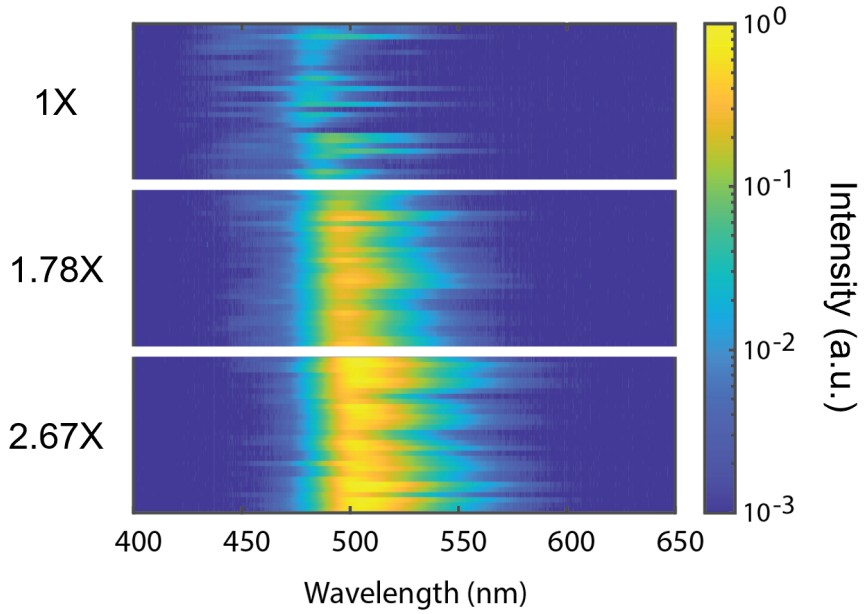

Figure 4-8. PL spectra for particles from (20,80,80) wells of three different well sizes.

displays the number of particles per well in (20,80,80) triangular wells of two different sizes as a function of contact angle θ. Since the positional accuracy definition cannot adequately account for empty wells, "particles per well" (PW) is applied as the metric for particle positioning. (In Sec. 4.3.2, we noted that 100% of particles from wells containing only one particle per well are found in the 20° angle, meaning that if $PW = 1$, high positional accuracy is expected. Comparatively, if $PW > 1$, low positional accuracy is expected due to presence of the secondary particles. PW therefore adequately accounts for the previously discussed scenarios (one or more particles per well), while enabling investigation of the empty well scenario.)

As previously explained, higher contact areas yield lower AM areas. At higher contact angles, we therefore expect the pressure gradient force to yield less directionality in positioning, and hence more erroneously positioned particles. Fig. 4-9 shows that particles per well increases with increasing contact angle, thus suggesting that nuclei are erroneously positioned during drainage. We note that the effect of contact angle is even more pronounced for the larger well size. This observation is consistent with

the presented theory, since in a laterally larger well, the distance d over which the meniscus is stretched is also larger, therefore yielding a smaller pressure gradient. In Fig. 4-9, we also see that particles per well decreases below 1 as contact angle decreases. At low contact angles, the molecular coverage of surfaces is expected to be more patch-like, which likely results in non-uniform wetting of wells. For precise positioning to be achieved, the contact angle must be chosen so as to limit secondary nucleations while also ensuring uniform filling of wells.

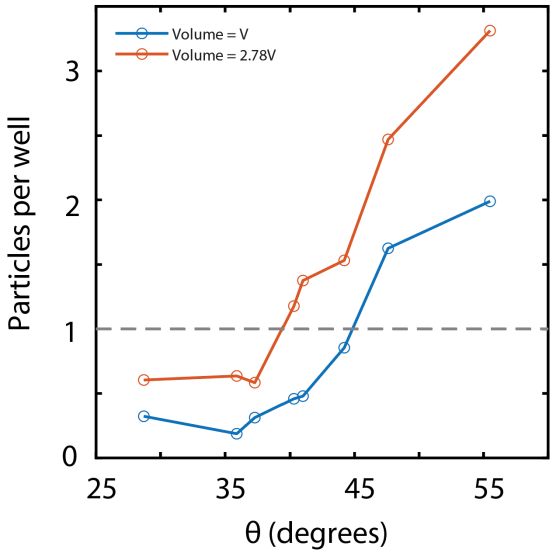

Figure 4-9. Particles per well (PW) for (20,80,80) triangles of two different well volumes, as a function of contact angle. The line at $PW = 1$ is provided as a visual aid.

4.4 Discussion

The results suggest that on-site, high-positional accuracy growth of nanocrystals can be achieved by tuning well geometry and sidewall contact angle. While we demonstrated growth of $CsPbBr_3$ nanocrystals, we expect the method to be applicable to other perovskite compositions, or even other non-perovskite salt-based nanocrystals. However, for growth of other materials to be realized, some additional optimization steps may be necessary. The extensions of this work will be explored in Chapter 5.

Chapter 5

Conclusion and Future Work

In this thesis, we demonstrated a method for on-site growth of halide perovskite nanocrystals with dimensions controlled down to <50 nm and sub-50 nm positional accuracy.

- In Chapter 2, we considered the properties of halide perovskites, and how those properties have precluded on-site growth with high positional accuracy using existing fabrication methods.
- In Chapter 3, we presented the theoretical framework behind our on-site growth method. We explored how asymmetric menisci yield asymmetric pressure gradients, which can be exploited for particle positioning. We then considered how asymmetric menisci can be controlled, and presented two parameters - well geometry and solvent contact angle - as critical to providing this control.
- In Chapter 4, we experimentally demonstrated that our method enables on-site growth of halide perovskite nanocrystals. We first showed that perovskite nanocrystals form in our lithographically-patterned wells. We next explored how varying the two identified parameters affects particle positioning. Finally, we investigated how nanocrystal structural and optical properties scale with well volume-scaling.

This work may be extended through a variety of means. Methods for passivating the particles may be investigated to increase the stability and quality of the nanocrystals. While colloidal nanocrystals are traditionally stabilized during synthesis (i.e. via presence of ligands in the precursor solution, which immediately bind to nanocrystals upon their formation [8]), our nanocrystals are currently not passivated. However, our crystals likely can be passivated via solution-phase deposition of molecular layers upon crystal growth, vapor-phase deposition of oxides (a method that has been explored for fabricating high-efficiency perovskite solar cells [31]), or deposition of other passivating agents.

Additional studies may also investigate how this method can be applied to other material systems (whether perovskite-based or not), like by varying the precursors, solvents, and growth conditions. For example, mixed solution and vapor-phase perovskite growth may be achieved by first applying our solution-based growth method to precisely position the seed crystal, and then performing vapor-phase deposition to transform the seed into a perovskite crystal. However, for our method to be successfully extended, the relative rates of evaporation (dictated by the solvent of choice, and temperature and pressure of the surroundings) and nucleation (dictated by the saturation state of the precursor solution, and evaporation rate of the solvent) in the new system must be understood and controlled, since these will affect the dynamics of particle positioning.

Appendix A

Appendix to Chapter 2

The well volume required to contain sufficient precursor solution to form a $CsPbBr_3$ orthorhombic nanocrystal of a given size can be calculated using Eqn. A.1. The parameters used and results are shown in Table A.1. Filling fraction is defined by Eqn. A.2.

Table A.1. Volumes and filling fractions of wells used to confine $CsPbBr_3$ precursor solution.

Parameter	**Unit**	**Value**
Volume of unit cell, V_{UC}	$Å^3$	793 [1]
Solution molarity, M	M	0.45 [1]
Volume of $CsPbBr_3$ crystal, $V_{crystal}$ of dimensions (35 nm, 35 nm, 20 nm)	nm^3	2.4500×10^4
Required well volume, V_{well}	nm^3	4.5596×10^5
Volume of well of dimensions (150 nm, 150 nm, 22 nm), V_{150}	nm^3	$4.950\,00 \times 10^5$
Filling fraction for V_{150}	–	0.9211
Volume of well of dimensions (100 nm, 100 nm, 22 nm), V_{100}	nm^3	$2.200\,00 \times 10^5$
Filling fraction for V_{100}	–	2.0726

[1]The solubility limit of $CsPbBr_3$ is ~ 0.5 M [32], so the molarity of the precursor solution used for solution-phase deposition must be < 0.5 M.

$$V_{crystal}\text{nm}^3 * \frac{10^3\text{Å}^3}{1\text{nm}^3} * \frac{1 \text{ unit cell}}{V_{UC}\text{Å}^3} * \frac{4 \text{ molecules}}{1 \text{ unit cell}} * \frac{1\text{mol}}{N_A \text{ molecules}} * \frac{1\text{L}}{M\text{mol}} * \frac{0.001\text{m}^3}{1\text{L}} * \frac{(10^9)^3\text{nm}^3}{\text{m}^3} \quad \text{(A.1)}$$

$$\text{Filling fraction} = \frac{V_{crystal}}{V_{well}} \quad \text{(A.2)}$$

These results suggest that V_{150} is large enough to form a crystal of size $V_{crystal}$, but V_{100} is not.

Appendix B

Appendix to Chapter 3

The capillary length is a characteristic length at which capillary forces become comparable to gravity forces. Below the capillary length, surface tension dominates over gravity. The relative importance of gravitational forces in capillary wetting can therefore be determined by considering the capillary lengths for various solvents. Capillary length is expressed by

$$\lambda = \sqrt{\frac{\gamma}{\rho g}} \tag{B.1}$$

where γ is the surface tension of the fluid, ρ is the fluid density, and g is the gravitational acceleration constant [33]. Capillary lengths for common solvents are presented in Table B.1. For all solvents, $\lambda \approx 2$ mm. This suggests that gravitational forces within the system of study (wells formed by 22 nm HSQ) are negligible.

Table B.1. Surface tensions, densities, and capillary lengths of solvents of interest at 20 °C.

Solvent	**Surface tension at solvent- air interface** γ(mN/m) [34]	**Density** (kg/m^3) [35]	**Capillary length** λ (mm)
Water	72.94	1000	2.73
Dimethyl sulfoxide (DMSO)	43.54	1092	2.02
Ethanol	22.39	789	1.70
Toluene	28.52	867	1.83

Appendix C

Appendix to Chapter 4

To understand why the equilateral triangle well has a larger value of positional accuracy than a square well of equivalent area, consider Fig. C-1. Each well contains one particle per corner (blue). Positional accuracy is evaluated by measuring the mean displacement from the indicated corner.

The positional accuracy for the square well is given by

$$A_{sq} = \frac{a + a + a\sqrt{2} + 0}{4} = \frac{a(2 + \sqrt{2})}{4} \tag{C.1}$$

The positional accuracy for the equilateral triangle well is given by

$$A_{tri} = \frac{b + b + 0}{3} = \frac{2b}{3} \tag{C.2}$$

For an equilateral triangle of side length b to have the same area as a square of side of length a, then

$$b = \frac{2a}{3^{1/4}} \tag{C.3}$$

Therefore, upon substitution, we find

$$\frac{A_{tri}}{A_{sq}} \approx 1.1869 \tag{C.4}$$

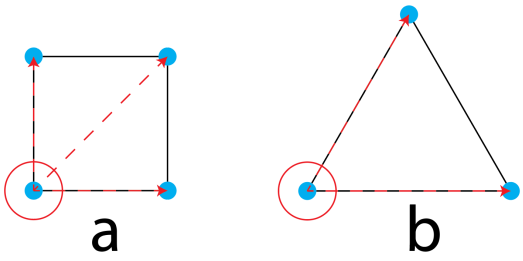

Figure C-1. Square well of length a and equilateral triangle well of length b. The area of the wells is equivalent.

Bibliography

[1] K. Chen, S. Schünemann, S. Song, and H. Tüysüz, "Structural effects on optoelectronic properties of halide perovskites," *Chemical Society Reviews*, vol. 47, no. 18, pp. 7045–7077, 2018.

[2] G. T. Smedley, *A Study of Immiscible Liquids, Liquid Behavior at Zero Gravity, and Dynamic Contact Lines and Angles*. PhD thesis, California Institute of Technology, 1990.

[3] P. Jia, M. Dong, and L. Dai, "Threshold pressure in arbitrary triangular tubes using RSG concept for all wetting conditions," *Colloids and Surfaces A: Physicochemical and Engineering Aspects*, vol. 302, no. 1-3, pp. 88–95, 2007.

[4] V. P. Carey and A. P. Wemhoff, "Disjoining pressure effects in ultra-thin liquid films in micropassages - Comparison of thermodynamic theory with predictions of molecular dynamics simulations," *Journal of Heat Transfer*, vol. 128, no. 12, pp. 1276–1284, 2006.

[5] W. J. Yin, T. Shi, and Y. Yan, "Unique properties of halide perovskites as possible origins of the superior solar cell performance," *Advanced Materials*, vol. 26, no. 27, pp. 4653–4658, 2014.

[6] J. S. Manser, J. A. Christians, and P. V. Kamat, "Intriguing Optoelectronic Properties of Metal Halide Perovskites," *Chemical Reviews*, vol. 116, no. 21, pp. 12956–13008, 2016.

[7] X. Zhang, M. E. Turiansky, J. X. Shen, and C. G. Van De Walle, "Defect tolerance in halide perovskites: A first-principles perspective," *Journal of Applied Physics*, vol. 131, no. 9, 2022.

[8] A. Dey, J. Ye, A. De, E. Debroye, S. K. Ha, E. Bladt, A. S. Kshirsagar, Z. Wang, J. Yin, Y. Wang, L. N. Quan, F. Yan, M. Gao, X. Li, J. Shamsi, T. Debnath, M. Cao, M. A. Scheel, S. Kumar, J. A. Steele, M. Gerhard, L. Chouhan, K. Xu, X.-g. Wu, Y. Li, Y. Zhang, A. Dutta, C. Han, I. Vincon, A. L. Rogach, A. Nag, A. Samanta, B. A. Korgel, C.-j. Shih, D. R. Gamelin, D. H. Son, H. Zeng, H. Zhong, H. Sun, H. V. Demir, I. G. Scheblykin, J. K. Stolarczyk, J. Z. Zhang, J. Feldmann, J. Hofkens, J. M. Luther, P. Julia, L. Li, L. Manna, M. I. Bodnarchuk, M. V. Kovalenko, M. B. J. Roe, N. Pradhan, O. F. Mohammed, O. M. Bakr, P. Yang, P. Mu, P. V. Kamat, Q. Bao, Q. Zhang, R. Krahne,

R. E. Galian, S. D. Stranks, S. Bals, V. Biju, W. A. Tisdale, Y. Yan, R. L. Z. Hoye, and L. Polavarapu, "State of the Art and Prospects for Halide Perovskite Nanocrystals," *ACS Nano*, vol. Article AS, 2021.

[9] L. Protesescu, S. Yakunin, M. I. Bodnarchuk, F. Krieg, R. Caputo, C. H. Hendon, R. X. Yang, A. Walsh, and M. V. Kovalenko, "Nanocrystals of Cesium Lead Halide Perovskites (CsPbX3, X = Cl, Br, and I): Novel Optoelectronic Materials Showing Bright Emission with Wide Color Gamut," *Nano Letters*, vol. 15, no. 6, pp. 3692–3696, 2015.

[10] G. Mannino, I. Deretzis, E. Smecca, A. L. Magna, A. Alberti, D. Ceratti, and D. Cahen, "Temperature-Dependent Optical Band Gap in CsPbBr 3 , MAPbBr 3 , and FAPbBr 3 Single Crystals," *Journal of Physical Chemistry C*, vol. 11, pp. 2490–2496, 2020.

[11] L. Brus, "Electronic wave functions in semiconductor clusters: Experiment and theory," *Journal of Physical Chemistry*, vol. 90, no. 12, pp. 2555–2560, 1986.

[12] J. S. Du, D. Shin, T. K. Stanev, C. Musumeci, Z. Xie, Z. Huang, M. Lai, L. Sun, W. Zhou, N. P. Stern, V. P. Dravid, and C. A. Mirkin, "Halide perovskite nanocrystal arrays: Multiplexed synthesis and size-dependent emission," *Science Advances*, vol. 6, no. 39, pp. 1–10, 2020.

[13] B. Jeong, H. Han, and C. Park, "Micro- and Nanopatterning of Halide Perovskites Where Crystal Engineering for Emerging Photoelectronics Meets Integrated Device Array Technology," *Advanced Materials*, vol. 32, no. 30, pp. 1–35, 2020.

[14] C. K. Lin, Q. Zhao, Y. Zhang, S. Cestellos-Blanco, Q. Kong, M. Lai, J. Kang, and P. Yang, "Two-Step Patterning of Scalable All-Inorganic Halide Perovskite Arrays," *ACS Nano*, vol. 14, no. 3, pp. 3500–3508, 2020.

[15] X. He, P. Liu, H. Zhang, Q. Liao, J. Yao, and H. Fu, "Patterning Multicolored Microdisk Laser Arrays of Cesium Lead Halide Perovskite," *Advanced Materials*, vol. 29, no. 12, 2017.

[16] J. Feng, X. Yan, Y. Zhang, X. Wang, Y. Wu, B. Su, H. Fu, and L. Jiang, ""Liquid Knife" to Fabricate Patterning Single-Crystalline Perovskite Microplates toward High-Performance Laser Arrays," *Advanced Materials*, vol. 28, no. 19, pp. 3732–3741, 2016.

[17] G. Wang, D. Li, H. C. Cheng, Y. Li, C. Y. Chen, A. Yin, Z. Zhao, Z. Lin, H. Wu, Q. He, M. Ding, Y. Liu, Y. Huang, and X. Duan, "Wafer-scale growth of large arrays of perovskite microplate crystals for functional electronics and optoelectronics," *Science Advances*, vol. 1, no. 9, pp. 1–9, 2015.

[18] L. Jibril, P. C. Chen, J. Hu, T. W. Odom, and C. A. Mirkin, "Massively Parallel Nanoparticle Synthesis in Anisotropic Nanoreactors," *ACS Nano*, vol. 13, no. 11, pp. 12408–12414, 2019.

[19] G. Mason and N. R. Morrow, "Capillary behavior of a perfectly wetting liquid in irregular triangular tubes," *Journal of Colloid and Interface Science*, vol. 141, no. 1, pp. 262–274, 1991.

[20] B. Camassel, N. Sghaier, M. Prat, and S. B. Nasrallah, "Evaporation in a capillary tube of square cross-section: Application to ion transport," *Chemical Engineering Science*, vol. 60, no. 3, pp. 815–826, 2005.

[21] J. N. Israelachvili, *Intermolecular and Surface Forces*. Boston: Elsevier, 3rd ed., 2011.

[22] H. Takagishi, T. Masuda, T. Shimoda, R. Maezono, and K. Hongo, "Method for the Calculation of the Hamaker Constants of Organic Materials by the Lifshitz Macroscopic Approach with Density Functional Theory," *Journal of Physical Chemistry A*, vol. 123, no. 40, pp. 8726–8733, 2019.

[23] M. Asbahi, Z. Dong, F. Wang, M. S. Saifullah, J. K. Yang, and K. S. Chong, "Second order directed positioning of nanoparticles induced by the main terminal meniscus shape in irregular template cavities," *Nanoscale*, vol. 9, no. 28, pp. 9886–9892, 2017.

[24] N. R. Mason, G. Morrow, "Meniscus Configurations and Curvatures in Non-Axisymmetric Pores of Open and Closed Uniform Cross Section," *Proceedings of the Royal Society of London, Series A, Mathematical and Physical Sciences*, vol. 414, no. 1846, pp. 111–133, 1987.

[25] S. H. Collicott and M. M. Weislogel, "Computing Existence and Stability of Capillary Surfaces Using Surface Evolver," *AIAA Journal*, vol. 42, no. 2, pp. 289–295, 2004.

[26] S. Son, L. Chen, Q. Kang, D. Derome, and J. Carmeliet, "Contact Angle Effects on Pore and Corner Arc Menisci in Polygonal Capillary Tubes Studied with the Pseudopotential Multiphase Lattice Boltzmann Model," *Computation*, vol. 4, no. 12, pp. 1–18, 2016.

[27] J. K. W. Yang and K. K. Berggren, "Using high-contrast salty development of hydrogen silsesquioxane for sub-10-nm half-pitch lithography," *Journal of Vacuum Science & Technology B: Microelectronics and Nanometer Structures*, vol. 25, no. 6, p. 2025, 2007.

[28] A. Stalder, "DropSnake and LB-ADSA user manual." 2011.

[29] A. F. Stalder, T. Melchior, M. Müller, D. Sage, T. Blu, and M. Unser, "Low-bond axisymmetric drop shape analysis for surface tension and contact angle measurements of sessile drops," *Colloids and Surfaces A: Physicochemical and Engineering Aspects*, vol. 364, no. 1-3, pp. 72–81, 2010.

[30] "Energy table for EDS analysis."

[31] J. A. Raiford, S. T. Oyakhire, and S. F. Bent, "Applications of atomic layer deposition and chemical vapor deposition for perovskite solar cells," *Energy and Environmental Science*, vol. 13, no. 7, pp. 1997–2023, 2020.

[32] Y. Rakita, N. Kedem, S. Gupta, A. Sadhanala, V. Kalchenko, M. L. Böhm, M. Kulbak, R. H. Friend, D. Cahen, and G. Hodes, "Low-Temperature Solution-Grown CsPbBr3 Single Crystals and Their Characterization," *Crystal Growth and Design*, vol. 16, no. 10, pp. 5717–5725, 2016.

[33] J. Feng and J. P. Rothstein, "Simulations of novel nanostructures formed by capillary effects in lithography," *Journal of Colloid and Interface Science*, vol. 354, no. 1, pp. 386–395, 2011.

[34] A. W. Adamson and A. P. Gast, *Physical Chemistry of Surfaces*. New York: John Wiley & Sons, Inc, 6th ed., 1997.

[35] B. J. Myers, "Common Solvents Used in Organic Chemistry: Table of Properties," 2021.